

Banner appropriate to article type will appear here in typeset article

Characterization of sea ice kinematics over oceanic eddies

Minki Kim¹, Georgy E. Manucharyan², and Monica M. Wilhelmus¹†

¹Center for Fluid Mechanics, School of Engineering, Brown University, Providence, RI 02912, USA

²School of Oceanography, University of Washington, Seattle, WA, USA

(Received xx; revised xx; accepted xx)

Eddies within the meso/submeso-scale range are prevalent throughout the Arctic Ocean, playing a pivotal role in regulating freshwater budget, heat transfer, and sea ice transport. While observations have suggested a strong connection between the dynamics of sea ice and the underlying turbulent flows, quantifying this relationship remains an ambitious task due to the challenges of acquiring concurrent sea ice and ocean measurements. Recently, an innovative study using a unique algorithm to track sea ice floes showed that ice floes can be used as vorticity-meters of the ocean. Here, we present a numerical and analytical evaluation of this result by estimating the kinematic link between free-drifting ice floes and underlying ocean eddies using idealized vortex models. These analyses are expanded to explore local eddies in quasi-geostrophic turbulence, providing a more realistic representation of eddies in the Arctic Ocean. We find that in both flow fields, the relationship between floe rotation rates and ocean vorticity depends on the relative size of the ice floe to the eddy. As the floe size approaches and exceeds the eddy size, the floe rotation rates depart from half of the ocean vorticity. Finally, the effects of ice floe thickness, atmospheric winds, and floe-floe collisions on floe rotations are investigated. The derived relations and floe statistics set the foundation for leveraging remote sensing observations of floe motions to characterize eddy vorticity at small to moderate scales. This innovative approach opens new possibilities for quantifying Arctic Ocean eddy characteristics, providing valuable inputs for more accurate climate projections.

Key words: Sea ice, Oceanic eddies, Marginal Ice Zones

1. Introduction

Subsurface mesoscale and submesoscale oceanic eddies, ranging from 10 to 300 km and 0.2 to 20 km, respectively, are widespread throughout the global ocean. These coherent structures are known to contain approximately 80% of the ocean kinetic energy (Ferrari & Wunsch 2009; Chelton *et al.* 2011; Morrow & Le Traon 2012), influencing global ocean circulation, biogeochemical tracer transport, and energy transfer across various length scales.

† Email address for correspondence: mmwilhelmus@brown.edu

Abstract must not spill onto p.2

Ocean turbulence at these scales typically follows the principles of geostrophic turbulence, characterized by an inverse energy cascade that strengthens larger eddies and redistributes kinetic energy and by a forward enstrophy cascade that creates finer filament features in the flow (Boffetta & Ecke 2012; Callies *et al.* 2015; Klein *et al.* 2019). In ice-covered regions, such as the Arctic Ocean, the characteristics of ocean turbulence are distinct; oceanic eddies contribute to sea ice melting by enhancing vertical mixing and transporting heat from deep ocean layers to the surface (Manucharyan & Thompson 2022c). In addition, atmosphere-sea ice-ocean interactions lead to momentum and heat exchanges, resulting in increased dissipation of eddy kinetic energy due to sea ice-ocean drag (Liu *et al.* 2024; Müller *et al.* 2024).

With the continued global warming trend, the Arctic sea ice cover has experienced changes in its characteristics and a rapid decline in its extent (Kwok & Rothrock 2009; Rampal *et al.* 2009; Comiso 2012; Yang *et al.* 2023; Howell *et al.* 2023). As a result, Arctic marginal ice zones (MIZ)—the transitional regions between dense pack ice and open ocean—have become more prominent (Strong & Rigor 2013; Rolph *et al.* 2020), fostering more energetic mesoscale variability in the ocean (Armitage *et al.* 2020; von Appen *et al.* 2022), and intensifying eddy fields (Manucharyan *et al.* 2022a). However, the variability of MIZ eddies and their relation to sea ice are yet to be fully characterized, partly due to the challenges of acquiring observations in ice covered regions. On the one hand, while in-situ field measurements, as those acquired via Ice-Tethered Profilers (Timmermans *et al.* 2008; Zhao *et al.* 2016) and moorings (Zhao *et al.* 2016; Pnyushkov *et al.* 2018; Cassianides *et al.* 2021), provide accurate, temporally resolved data, measurements remain sparse and mostly out of MIZ. On the other hand, remote sensing techniques, including satellite altimetry, offer broader spatial coverage and allow for a more comprehensive characterization of the eddy field (Kubryakov *et al.* 2021). But, processing data in ice-covered areas remains challenging, limiting analyses to seasonally ice-free regions. In addition, satellite altimeters acquire measurements infrequently and with limited spatial coverage at high latitudes, where the Rossby deformation radius is smaller compared to lower latitudes. Notably, the recent launch of the Surface Water and Ocean Topography satellite, with $O(1\text{ km})$ spatial resolution, promises more detailed surface velocity information from altimetry observations (Dibarboure *et al.* 2024). However, methodologies for deriving surface velocities from sea surface height are still under development and not yet fully operational.

Analysis of remote sensing sea ice imagery has been proposed as a unique alternative to standard techniques for the characterization of the turbulent eddy field in MIZ, albeit qualitatively. The first description of subsurface ocean eddies imprinted on ice edges in the Fram Strait MIZ was made using airborne remote sensing imagery (Johannessen *et al.* 1987). More recently, studies employing Synthetic Aperture Radar (SAR) images have detected the distinct signature of ocean eddies and filaments on the distribution of sea ice, enabling the quantification of eddy counts, sizes, and positions (Kozlov *et al.* 2019; Cassianides *et al.* 2021; Kozlov & Atadzhanova 2022). Similarly, under-ice eddy characteristics have been inferred through Lagrangian observations of ice floe rotation rates (Manucharyan *et al.* 2022a), retrieved from Moderate Resolution Imaging Spectroradiometer (MODIS) optical imagery (Lopez-Acosta *et al.* 2019). This study demonstrated that upper ocean eddy vorticity has a tight link to ice floe rotations via ice-ocean torques, as atmospheric winds primarily drive ice floe advection, resulting in persistent daily-scale floe rotations.

From a fundamental standpoint, fluid flows have long been characterized using micro-size particles as tracers. Inertialess spherical particles, for instance, serve as idealized passive tracers, effectively measuring flow fields via particle image velocimetry (Adrian & Westerweel 2011). However, different particle properties (e.g., inertia, shape, size) result in distinct behaviors. Particle inertia causes a delayed response to changes in the flow fields,

leading to misalignment between particle motion and the background flow field (Mortensen *et al.* 2007; Ouellette *et al.* 2008; Zhao *et al.* 2015; Brandt & Coletti 2022). In turbulent shear flows, particle inertia can enhance rotational motion, especially near walls (Mortensen *et al.* 2007). Ouellette *et al.* (2008) also demonstrated that Lagrangian measurements of inertial particles along their trajectories differ from those of passive tracers in chaotic flows. In addition, inertial particles with different sizes and shapes exhibit unique rotational behaviors induced by local velocity gradients in various types of turbulent flows (Voth & Soldati 2017; Brandt & Coletti 2022), including homogeneous isotropic turbulence (Bordoloi & Variano 2017; Allende & Bec 2023), turbulent channel flow (Zhao *et al.* 2015), and turbulent boundary layers (Tee & Longmire 2024). These cumulative findings not only advance our fundamental understanding of particle dynamics but also suggest a promising potential for using particles to characterize a wide range of flow fields.

In systems where only a limited number of seeded particles are accessible, Lagrangian approaches can retrieve flow structure, and examples span cryogenic (Švančara *et al.* 2020) and environmental flows (Dauxois *et al.* 2021). For instance, in flows involving superfluid ^4He , where only 100 particles can be detected within a 1 MPixel image, Outrata *et al.* (2021) employed Lagrangian particles to determine the vorticity of vortex rings. Similarly, in the MIZ, the number of ice floes is limited, making it challenging to fully resolve the underlying ocean fields. Ice floes also integrate surface ocean stresses, filtering out information and reflecting local ocean information. Tracking individual ice floes may offer a valuable opportunity for quantifying ocean field characteristics. In addition, recent efforts have been aimed at characterizing coherent structures and even flow fields using sparse trajectories of particles (Mowlavi *et al.* 2022; Harms *et al.* 2023) and ice floes (Covington *et al.* 2022). These cumulative findings in fluid mechanics with particles imply the potential of particle tracking to measure fluid vorticity, suggesting that sea ice could serve as an effective tracer for quantifying ocean flow fields.

In this study, we explore the kinematic relationship between ice floes and underlying ocean eddies, focusing specifically on the role of ice floe size relative to eddy size. We employ ocean eddy models (Arbic *et al.* 2012) and ice floe models (Manucharyan & Montemuro 2022b; Montemuro & Manucharyan 2023) for ice floe-ocean simulations. Ice floe rotation in an idealized ocean vortex is examined, and analytical relations for ice floe rotation are introduced in §3.2. The potential applicability of these analyses to more realistic ocean conditions is also discussed in §3.3. The effects of key factors, such as ice floe thickness (§4.1), atmospheric winds (§4.2), floe-floe collisions, and sea ice concentration (§4.3), on the rotational relationship are examined in §4.

2. Methods

2.1. Ocean eddy models

Two numerical models were employed to generate idealized ocean flow fields: (a) the Taylor-Green (TG) vortex and (b) a two-layer quasi-geostrophic (QG) model. We describe the key details of the TG and QG simulations in turn. Simulation parameters for the two models are summarized in table 1.

The TG vortex is an idealized two-dimensional flow field frequently employed in the literature due to its exact closed-form solutions for incompressible flows. For example, it has been used as a background flow field in studies of multiphase flows to investigate the motion of particles (Wereley & Lueptow 1999; Qiao *et al.* 2015; Jayaram *et al.* 2020), bubbles (Deng *et al.* 2006), and droplets (Qiao *et al.* 2014) in idealized flow settings. Here, we examine the motion of ice floes over a TG vortex and derive analytical expressions for their relationship.

Table 1: Parameters and properties for ocean eddy (top) and ice floe (bottom) models.

Parameter	Symbol	Definition	Value
Amplitude of stream function (TG)	A_{TG}	—	$1.23 \times 10^3 \text{ m}^2/\text{s}$
Size of a vortex cell (TG)	L_{TG}	—	35 km
Domain size (QG)	L_{QG}	—	400 km
Rossby radius of deformation (QG)	L_d	—	5.2 km
Ratio of layer depths (QG)	δ	H_1/H_2	1
Vertical shear of horizontal currents (QG)	ΔU	$U_1 - U_2$	0.21 m/s
Effective drag length scale (QG)	r_1	$C_{d,eff}/H_1$	$2 \times 10^5 \text{ m}^{-1}$
Linear dissipation time scale (QG)	r_2	—	0.01 days^{-1}
Density (ocean)	ρ_o	—	1027 kg/m ³
Density (ice floe)	ρ_f	—	920 kg/m ³
Density (atmosphere)	ρ_a	—	1.2 kg/m ³
Sea ice-ocean drag coefficient	$C_{d,o}$	—	5.5×10^{-3}
Sea ice-atmosphere drag coefficient	$C_{d,a}$	—	1.0×10^{-3}
Turning angle (ocean)	θ_o	—	15°
Turning angle (atmosphere)	θ_a	—	0°
Radius (ice floe)	R_f	—	1–35 km
Thickness (ice floe)	h_f	—	0.1–1.0 m
Young’s modulus (floe collisions)	E_f	—	$5 \times 10^7 \text{ Pa}$
Shear modulus (floe collisions)	G_f	$E_f/2(1 + \nu)$	$1.9 \times 10^7 \text{ Pa}$
Poisson’s ratio (floe collisions)	ν	—	0.3
Speed (atmosphere)	$ \mathbf{u}_a $	—	0–12 m/s
Coriolis parameter	f	—	10^{-4} s^{-1}
Non-dimensionalized floe inertia	$H_{f,o}^*$	$\rho_f h_f / \rho_o C_{d,o} L_o$	$10^{-3} - 10^{-2}$
Rossby number	Ro	$U_o / f L_o$	0.045
Nansen number	Na	$\sqrt{\rho_a C_{d,a} / \rho_o C_{d,o}}$	0.015

We consider a TG vortex cell of size L_{TG} centered at the origin. The stream function of the square-shaped TG vortex is given by

$$\psi_{TG} = -A_{TG} \cos\left(\frac{\pi x}{L_{TG}}\right) \cos\left(\frac{\pi y}{L_{TG}}\right), \quad (2.1)$$

where A_{TG} is the amplitude, and x and y are the spatial coordinates. Maximum vorticity magnitude occurs at the vortex center, gradually decreasing radially outward until reaching zero at the boundary of the vortex cell. Without loss of generality, we consider only the cyclonic case. Both anticyclonic and cyclonic eddies are present in the Arctic Ocean, yet for the results derived here, the anticyclonic and cyclonic cases differ only in sign.

The two-layer QG model produces more realistic ocean eddies similar in size and shape to those observed in the MIZ. We employed the QG flow field tuned to observations from the Beaufort Sea (Manucharyan *et al.* 2022a). Full details of the model and the tuning of its parameters can be found in Arbic *et al.* (2012) and Manucharyan *et al.* (2022a). The QG model setup divides the ocean into two vertical layers that are assumed to be homogeneous in the horizontal direction. The vertically sheared horizontal flows in these two layers induce a baroclinic instability, resulting in the generation of eddies evolving over the horizontal plane of each layer, which is the most common eddy generation mechanism in the global ocean (Tulloch *et al.* 2011), including the Arctic BG (Hunkins 1974; Manucharyan & Stewart 2022).

In both layers, the mean horizontal velocity is imposed in the zonal direction U , leading to gradients in the mean potential vorticity, Q , which accounts for vorticity with the presence of stratification. These velocity and vorticity gradients result in zonal (x) and meridional (y) velocity perturbations (u and v) as well as potential vorticity perturbation (q). The evolution of the perturbation vorticity fields in each layer is described by the QG equations, which account for the Coriolis force and the vertical shear of the velocity. The governing equations for each layer are as follows:

$$\frac{\partial q_1}{\partial t} + (u_1 + U_1) \frac{\partial q_1}{\partial x} + v_1 \frac{\partial q_1}{\partial y} = -v_1 \frac{\partial Q_1}{\partial y} - r_1 |\nabla \times \mathbf{u}_1| |\mathbf{u}_1| + s.s.d., \quad (2.2)$$

$$\frac{\partial q_2}{\partial t} + (u_2 + U_2) \frac{\partial q_2}{\partial x} + v_2 \frac{\partial q_2}{\partial y} = -v_2 \frac{\partial Q_2}{\partial y} - r_2 \nabla^2 \psi_2 + s.s.d., \quad (2.3)$$

where subscripts 1 and 2 denote the top and bottom layers, respectively, t is the time, \mathbf{u} is the vector form of the perturbed velocity, $r_1 = C_{d,eff}/H_1$ stands for the effective drag length scale for the top layer, $C_{d,eff}$ is the effective sea ice-ocean drag coefficient, H is the layer depth, r_2 is the linear dissipation time scale for the bottom layer, ψ is the perturbation stream function, and $s.s.d.$ is small-scale dissipation using an exponential cutoff filter. In this set of equations, the uniform dissipation caused by the quadratic sea ice-ocean drag is incorporated in the top layer, while Ekman-type friction is included in the bottom layer. Small-scale dissipation is also considered to prevent a forward-entropy cascade towards small scales. The imposed mean potential vorticity gradients are given by:

$$\frac{\partial Q_1}{\partial y} = \frac{U_1 - U_2}{(1 + \delta)L_d^2}, \quad \frac{\partial Q_2}{\partial y} = \frac{\delta(U_2 - U_1)}{(1 + \delta)L_d^2}, \quad (2.4)$$

where $\delta = H_1/H_2$ is the ratio of layer depths, L_d is the Rossby radius of deformation, and $\Delta U = U_1 - U_2$ is the vertical shear of horizontal currents. The perturbation potential vorticities in the two layers are given by:

$$q_1 = \nabla^2 \psi_1 + \frac{\psi_2 - \psi_1}{(1 + \delta)L_d^2}, \quad q_2 = \nabla^2 \psi_2 + \frac{\delta(\psi_1 - \psi_2)}{(1 + \delta)L_d^2}. \quad (2.5)$$

The model uses an f -plane approximation since the Coriolis parameter is approximately constant in the Arctic Ocean (Timmermans & Marshall 2020).

The simulation domain spans $400 \text{ km} \times 400 \text{ km}$ and is set up with doubly-periodic boundary conditions. Time integration was performed using the Adams-Bashforth two-step method in Fourier space with 256 modes, producing a converged energy spectrum previously validated by Manucharyan *et al.* (2022a). The model was initialized with randomly generated q_1 and q_2 in Fourier space. The simulation was conducted until the flow field reached an equilibrated state. At that point the energy production from the mean flow was balanced by the energy dissipation from the top and bottom layers due to the sea ice-ocean drag and the Ekman drag, respectively. This equilibration state is typically achieved after approximately one simulation year. The model tuning parameters, L_d , δ , and ΔU , were adopted from Manucharyan *et al.* (2022a). As a result, the simulated eddy fields closely matched the statistics of the Beaufort Gyre MIZ between 2003 and 2020. It is important to note that the sizes of the produced eddies are within the observed range of the eddy sizes (on the order of 10 km) in the MIZ (Johannessen *et al.* 1987; Kozlov *et al.* 2019; Kozlov & Atadzhanova 2022). In addition, the estimated eddy kinetic energy derived from the simulated ice floes is comparable to the estimated eddy kinetic energy from in situ measurements via moorings located in the area of the satellite observations (Manucharyan *et al.* 2022a).

Arctic MIZ eddies typically persist for a period of $O(10)$ days (Johannessen *et al.* 1987;

Kozlov *et al.* 2020; Cassianides *et al.* 2021; Kozlov & Atadzhanova 2022); hence, we consider stationary ocean fields during the 30-day simulation period. Note that the simulation incorporates the effects of sea ice-ocean drag as an effective, continuous, stationary drag force over the top layer, influencing the energetics of the QG eddy field. The quadratic drag law is used due to the turbulent nature of the flow field, consistent with studies on the ice-ocean boundary layer (McPhee 2012; Cole *et al.* 2014). The effective sea ice-ocean drag coefficient represents the overall impact of drag forces on the ocean field, implying the product of sea ice concentration and the actual ice-ocean drag coefficient (Manucharyan & Stewart 2022). This constant coefficient neglects small-scale floe dynamics and seasonal variations. For the given Rossby radius, changes in the effective drag coefficient of less than 25% compared to the tuned value have negligible effects on the slope of the eddy energy spectrum. This implies that such variations in ice floe surface properties may have a limited impact on energy transport across scales.

While the tuning parameters in the QG model can produce consistent eddy energetics, local eddy sizes and velocities may vary, even for simulation runs set up with identical tuning parameters. Therefore, instead of covering a wide range of eddy sizes, we set the parameters in the TG vortex model according to the relative length scales of eddies and ice floes (table 1). The majority of the observed ice floe sizes range from 1 to 35 km (Manucharyan *et al.* 2022a). L_{TG} was set to broadly cover the floe-eddy size ratios from 0.05 to 2. Ratios higher than 2 were excluded, as these larger floes tend to filter out most of the eddy information and have a limited reflection of the local eddies underneath them. Concurrently, A_{TG} in equation 2.1, was chosen to represent the maximum velocity of local QG eddies corresponding to L_{TG} . These length and velocity scales fall within the ranges of observed eddy sizes (1–40 km) (Kozlov *et al.* 2019) and flow speeds (0–0.5 m/s) (Kozlov & Atadzhanova 2022) in the BG MIZ.

Finally, local eddies (or coherent vortices) in ocean flow fields are identified in this study by using the Lagrangian-averaged vorticity deviation (LAVD)-based approach proposed by Haller *et al.* (2016). We note that other identification schemes exist, such as the Okubo-Weiss parameter (Okubo 1970; Isern-Fontanet *et al.* 2004; Pérez-Muñuzuri & Huhn 2013), Lagrangian trajectory methods (Haller 2005; Dong *et al.* 2011), and others based on the values of sea surface heights, and vorticity (Chelton *et al.* 2011; Mason *et al.* 2014). We opted for the LAVD-based eddy detection method given that it is both time- and rotation-invariant and has demonstrated good performance in detecting coherent structures in altimeter-derived velocity fields of the global ocean (AVISO: Archiving, Validation and Interpretation of Satellite Oceanographic data) (Abernathey & Haller 2018; Liu & Abernathey 2023). More details are provided in §3.3.

2.2. Sea ice model

We simulate the motion of circular ice floes using the SubZero discrete element sea ice model (Manucharyan & Montemuro 2022b). This model is designed to study the behavior of ice floes under mechanical forcing. We parameterize the sea ice-ocean and sea ice-atmosphere stresses through a quadratic drag law (Leppäranta 2011):

$$\boldsymbol{\tau}_o = \rho_o C_{d,o} |\mathbf{u}_o - \mathbf{u}_i| e^{i\theta_o} (\mathbf{u}_o - \mathbf{u}_i), \quad \boldsymbol{\tau}_a = \rho_a C_{d,a} |\mathbf{u}_a - \mathbf{u}_i| e^{i\theta_a} (\mathbf{u}_a - \mathbf{u}_i), \quad (2.6)$$

where $\boldsymbol{\tau}$ is the shear stress, ρ is the density, θ is the turning angle, and the subscript o , a , and i correspond to the ocean, the atmosphere, and the ice floe, respectively. Since $\mathbf{u}_a \gg \mathbf{u}_i$, $(\mathbf{u}_a - \mathbf{u}_i) \approx \mathbf{u}_a$ was used. The ocean turning angle is the angle between the geostrophic current and the surface shear stress, as the Coriolis effect causes the flow to turn within the boundary layers. Here, \mathbf{u}_o represents the velocity of the geostrophic current beneath the Ekman layer (~ 20 m (Yang 2006; Ma *et al.* 2017)), with a direction rotated relative to the ocean surface

velocity by a turning angle of θ_o . The geostrophic velocity generally has larger magnitudes than the surface ocean velocity in the BG (Zhong *et al.* 2018). The wind turning angle is set to zero, as the surface wind is considered.

The velocity of ice floes comprises translational and rotational components, $\mathbf{u}_i = \mathbf{u}_f + \Omega_f \hat{\mathbf{k}} \times \mathbf{r}'$, where \mathbf{u}_i is the sea ice velocity over the ice floe area, \mathbf{u}_f is the translational velocity of the center-of-mass, Ω_f is the rotation rate of the ice floe, and $\mathbf{r}' = \mathbf{r} - \mathbf{r}_C$ is the position vector on the ice floe with respect to its center-of-mass, C . The translational velocity and rotation rate of ice floes evolve according to the linear and angular momentum conservation equations:

$$M_f \left(\frac{d\mathbf{u}_f}{dt} + f \hat{\mathbf{k}} \times \mathbf{u}_f \right) = \iint_A (\boldsymbol{\tau}_o + \boldsymbol{\tau}_a - \rho_f h_f g \nabla \eta) dA + \sum_{j,k} \mathbf{F}_{j,k}, \quad (2.7)$$

$$I_f \frac{d\Omega_f}{dt} = \iint_A \mathbf{r}' \times (\boldsymbol{\tau}_o + \boldsymbol{\tau}_a - \rho_f h_f g \nabla \eta) dA + \sum_{j,k} \mathbf{r}'_{j,k} \times \mathbf{F}_{j,k}, \quad (2.8)$$

where $M_f = \rho_f A_f h_f$ is the floe mass, ρ_f is the floe density, $A_f = \pi R_f^2$ is the floe area, h_f is the floe thickness, R_f is the floe radius, t is time, g is the gravitational acceleration, η is the sea surface height anomaly associated with ocean currents, A is the surface area covered by an ice floe, $\mathbf{F}_{j,k}$ is the interaction forces of the k th contact point with the j th ice floe due to collisions, $I_f = M_f R_f^2 / 2$ is the moment of inertia for a floe with an axis passing through the center-of-mass, and $\mathbf{r}'_{j,k} = \mathbf{r}_{j,k} - \mathbf{r}_C$ is the position vector on the k th contact point with the j th ice floe with respect to its center-of-mass. The left-hand side of (2.7) represents the rate of change of ice floe momentum and the Coriolis force acting on ice floes, while the integration terms on the right-hand side consist of the sea ice-ocean stress, the sea ice-atmosphere stress, and the pressure gradient due to the sea surface tilt. Equation (2.8) consists of the corresponding torque terms. Floe-floe collisions are neglected for ice floes subjected only to oceanic and wind forcings, resulting in $\mathbf{F}_{j,k} = 0$. While these floes can be more observable in regions with low sea ice concentrations, they effectively capture the key connections between ice floes and underlying eddies. In addition, it establishes a baseline for ice floe motions in regions with high concentrations. Free-drifting ice floes with no collisions are examined in most sections, while the effects of floe-floe collisions are discussed in §4.3.

Using the length L_o , velocity U_o , and time T_o scales of the ocean field, (2.7) and (2.8) can be rewritten in non-dimensionalized form:

$$\begin{aligned} \frac{d\mathbf{u}_f^*}{dt^*} &= \frac{1}{H_{f,o}^*} \iint_{A^*} |\mathbf{u}_o^* - \mathbf{u}_i^*| e^{i\theta_o} (\mathbf{u}_o^* - \mathbf{u}_i^*) dA^* \\ &+ \frac{Na^2}{H_{f,o}^*} \iint_{A^*} |\mathbf{u}_a^* - \mathbf{u}_i^*| (\mathbf{u}_a^* - \mathbf{u}_i^*) dA^* + \frac{1}{Ro} \iint_{A^*} \hat{\mathbf{k}} \times (\mathbf{u}_o^* - \mathbf{u}_f^*) dA^*, \end{aligned} \quad (2.9)$$

$$\begin{aligned} \frac{d\Omega_f^*}{dt^*} &= \frac{2}{R_f^{*2}} \left[\frac{1}{H_{f,o}^*} \iint_{A^*} \mathbf{r}'^* \times [|\mathbf{u}_o^* - \mathbf{u}_i^*| e^{i\theta_o} (\mathbf{u}_o^* - \mathbf{u}_i^*)] dA^* \right. \\ &\left. + \frac{Na^2}{H_{f,o}^*} \iint_{A^*} \mathbf{r}'^* \times [|\mathbf{u}_a^* - \mathbf{u}_i^*| (\mathbf{u}_a^* - \mathbf{u}_i^*)] dA^* + \frac{1}{Ro} \iint_{A^*} \mathbf{r}'^* \times (\hat{\mathbf{k}} \times \mathbf{u}_o^*) dA^* \right], \end{aligned} \quad (2.10)$$

where $H_{f,o}^* = \rho_f h_f / \rho_o C_{d,o} L_o$ is the non-dimensionalized floe inertia characterizing ice floe inertia relative to surface ocean drag, $Na = \sqrt{\rho_a C_{d,a} / \rho_o C_{d,o}}$ denotes the Nansen number, $Ro = U_o / f L_o$ denotes the Rossby number, $A^* = A / A_f$ is the non-dimensionalized

floe area, and the superscript * indicates non-dimensionalized quantities. Note that the sea surface height tilt terms in (2.7) and (2.8) are rewritten using $-g\nabla\eta = f\hat{\mathbf{k}} \times \mathbf{u}_o$, indicating the geostrophic balance between the pressure gradient force due to the sea surface tilt and the Coriolis force. Interaction forces due to floe-floe collisions are neglected in the non-dimensionalized forms.

Simulations with the SubZero model employ an Adams-Bashforth two-step method for time integration and a Monte-Carlo scheme (Caffisch 1998) at each time step for spatial integration of forces and torques acting on individual ice floes. The velocity and rotation rate of ice floes are initialized with the averaged values of ocean eddies beneath them. In this study, we excluded the first five days of simulation to eliminate any influence of initial conditions on the dynamics. An extensive description of the Subzero model can be found in Manucharyan & Montemuro (2022b); Montemuro & Manucharyan (2023). The codes associated with the model are available at <https://github.com/SeaIce-Math/SubZero>.

The physical properties of the ocean, sea ice, and the atmosphere used in the simulations are chosen based on geostrophic drag coefficients and turning angles specific to conditions in the Beaufort Gyre MIZ (table 1, from Leppäranta (2011) and Brenner *et al.* (2021)). We considered ice floes with sizes ranging from 1 to 35 km, covering most of the observations acquired in the BG MIZ from 2003 to 2000 (Manucharyan *et al.* 2022a). We removed the influence of shape variations on the rotational relationship between ice floes and the ocean by reducing observed floe geometries to circular shapes. This agrees with studies by Gupta & Thompson (2022), Brenner *et al.* (2023), and Gupta *et al.* (2024). The simulation time of 30 days is chosen to minimize any effects due to melt and sea ice-ocean interactions (Gupta & Thompson 2022). For non-dimensionalization, the size and the velocity amplitude of a TG vortex are taken as the reference length and velocity scales, respectively.

For the initial part of this study, we considered ice floes with a constant thickness of $h_f = 0.5$ m, in agreement with observed values in the BG MIZ (Krishfield *et al.* 2014; Timmermans & Marshall 2020; Manucharyan *et al.* 2022a). We also neglected atmospheric stresses. The effects of varying ice floe thickness and wind speeds on the rotational relationship between ice floes and underlying ocean eddies are presented in §4.1 and §4.2. Lastly, the passive tracer, devoid of inertia, perfectly follows the fluid, mirroring the local velocity and rotation of fluid flows. The passive tracer scenario serves as an idealized baseline case in our analysis.

3. Results

This section investigates the rotational relationship between ice floes and underlying ocean eddies for different floe-eddy size ratios in the TG vortex and two-layer QG flow fields. Two types of ocean quantities were explored for the analyses: (i) area-averaged ocean quantities, calculated by averaging ocean quantities over the ice floe area, representing localized ocean information in regions with ice floe coverage, and (ii) center-of-mass ocean quantities, obtained through the interpolation of quantities at the center-of-mass of the ice floe, offering pointwise ocean information. These two types of quantities are complementary; area-averaged quantities can be used to create spatial vorticity maps when sea ice concentration is high, while quantities derived from information at the center-of-mass can be leveraged to estimate ocean vorticity at lower concentrations, mainly when ice floes undergo a closed-loop trajectory over a larger area.

3.1. Single ice floe dynamics

The motion of individual ice floes with different sizes was analyzed in a TG vortex field and compared to the passive tracer case (figure 1). Three floe-eddy size ratios were considered, $R_f/R_e = 0.1, 0.5, 1.0$. In all cases, the center-of-mass of the ice floes was initially positioned

at $r_f = 0.5R_e$, where r_f denotes the radial position of the floe center-of-mass, to capture the influence of ocean fields both inside and outside the vortex cell.

The trajectories of free-drifting ice floes are shaped by ocean and atmospheric forcing, the effects of floe inertia, the Coriolis force, and the pressure gradient force due to the sea surface tilt. Under low to negligible wind speeds and low sea ice concentration, ice floe motion is expected to be predominantly driven by oceanic forcing. However, it has been hypothesized that ice floe inertia plays an important role in setting the direction in which floes translate by delaying their response to changes in the underlying ocean flow field. From the cases tested, the ice floe with a size ratio of $R_f/R_e = 0.5$ exhibited the best performance at resembling a passive tracer and forming a closed-loop trajectory over the TG vortex cell (figure 1a). While inertia does result in an outward tilt of the ice floe velocity $\mathbf{u}_f(t)$ relative to the ocean velocity averaged over the floe area at t , $\bar{\mathbf{u}}_o(t)$ (a subset of figure 1a), the resulting force from combining the Coriolis force and the pressure gradient force due to the sea surface tilt, $\hat{k} \times (\bar{\mathbf{u}}_o - \mathbf{u}_f)$, reduces this spiraling effect, effectively driving the ice floe to form a closed loop (figure 1a). Finally, ice floes were observed to undergo alternating periods of acceleration and deceleration relative to the equilibrium state in which all forces balance instantaneously to zero. As a result, the radial component of floe position oscillates with respect to the center of the vortex core, r_f (figure 1b).

Changes in floe size with respect to vortex size result in a deviation of floe motion with respect to the eddying motion underneath. For example, smaller ice floes, for which $R_f/R_e = 0.1$, followed an outwardly spiral trajectory. In this case, the ice floe velocity and the averaged ocean velocity vectors were better aligned, reducing the inward effect from the Coriolis and pressure gradient forces compared to floes with larger size ratios. This is similar to the behavior of millimeter-sized particles in a Taylor vortex (Wereley & Lueptow 1999; Deng *et al.* 2006; Qiao *et al.* 2015) and a Rankine vortex (Varaksin & Ryzhkov 2022), in which the role of inertia is linked to their resulting spiral trajectories relative to the flow direction. As the floe-eddy size ratio increases to $R_f/R_e = 1.0$, discrepancies between ice floe and averaged ocean velocities become more pronounced due to filtration of measured ocean velocities over larger floe areas. This results in larger forces directed toward the vortex center compared to smaller floes, leading to an inward spiraling motion.

The kinematics of ice floes with different sizes were examined along their trajectories (figure 2). We present results using two normalizations: (i) considering ocean quantities averaged over the floe area, including averaged ocean vorticity, $\bar{\omega}_o$, and averaged ocean speed, \bar{V}_o ; and (ii) ocean quantities at the floe center-of-mass, such as ocean vorticity, $\omega_{o,C}$, and ocean speed, $V_{o,C}$. Note that the floe rotation rates are normalized by half of the ocean vorticity. Angle deviations are calculated by subtracting the angle of the ocean velocity from that of the ice floe velocity, $\Delta\theta_f = \theta_f - \bar{\theta}_o$ and $\Delta\theta_{f,C} = \theta_f - \theta_{o,C}$, where θ_f denotes the angle of the ice floe velocity, $\bar{\theta}_o$ denotes the angle of the ocean velocity averaged over the ice floe area, and $\theta_{o,C}$ denotes the angle of the ocean velocity at the center of mass of the ice floe. All angles are calculated using the direction of each velocity vector with respect to the positive x -axis, measured in the counter-clockwise direction.

Normalized ice floe rotation rates, velocities, and orientations oscillated over time, periodically crossing the equilibrium values. Small ice floes with $R_f/R_e = 0.1$ show higher sensitivity to local ocean quantities, leading to normalized rotation rates and speeds close to unity and minimal angle deviations (figure 2). Ocean quantities averaged over the floe area and at the floe center-of-mass exhibit similar values, resulting in comparable normalized rotation rates (figure 2a, b) and speeds (figure 2c, d). As ice floes move farther from the vortex center along their outwardly spiral trajectories, the normalized rotation rates begin to decrease at later times. The angle deviations have negative values for most of the evolution

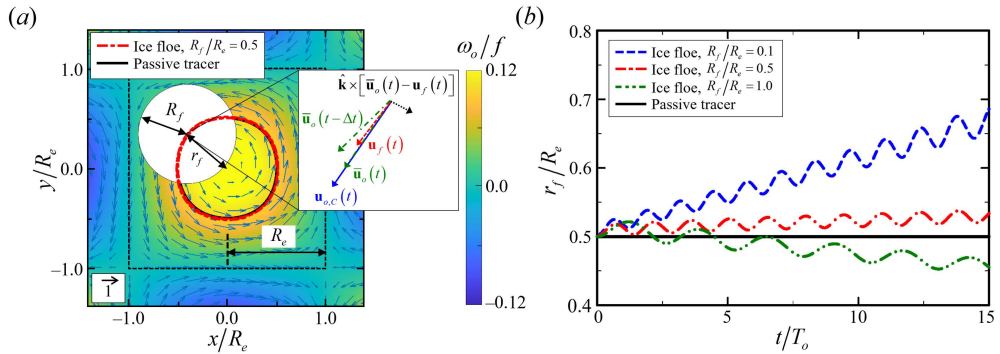


Figure 1: Ice floes drifting over a TG vortex field. (a) The trajectory of a circular ice floe released at the radial position, r_f , set to be half of the TG vortex size, R_e ($R_f/R_e = 0.5$). The colors map the magnitude of the fluid vorticity normalized by the Coriolis parameter, while the arrows indicate the direction of the fluid velocity (with the arrow size set to scale according to the velocity magnitude) at a given location. The inset schematic shows the orientation of relevant vectors: the ocean velocity averaged over the floe area, $\bar{\mathbf{u}}_o$, the ocean velocity at the center-of-mass of the floe, $\mathbf{u}_{o,C}$, the ice floe velocity at its center-of-mass, \mathbf{u}_f , and the force direction resulting from combining the Coriolis force and the pressure gradient force due to the sea surface tilt, $\hat{\mathbf{k}} \times (\bar{\mathbf{u}}_o - \mathbf{u}_f)$. (b) Radial positions of ice floes with floe eddy size ratios of $R_f/R_e = 0.1$ (blue dashed lines), 0.5 (red dot-dashed lines), and 1.0 (green double dot-dashed lines), normalized by the size of the eddy. The ice floe cases are compared to the passive tracer case (black solid lines).

time due to the outwardly spiral shape of the trajectory (2e, f). Contrasting the ice floe case, the passive tracer perfectly mirrors the vorticity and velocity of the underlying flow field with zero angle deviations.

As the floe-eddy size ratios increase to $R_f/R_e = 1.0$, the normalized ice floe rotation rates and speeds exhibit larger deviations from unity (figure 2a–d). With larger floe-eddy size ratios, the floe rotation rates normalized by the averaged ocean vorticity increase because the floe samples low-vorticity regions near cell boundaries, reducing the averaged ocean vorticity (figure 2a). Conversely, the floe speeds normalized by the averaged ocean speed decrease due to high-velocity regions near the cell boundaries covered by the floe area, resulting in higher averaged ocean speed (figure 2c). In the context of ocean quantities at the floe center-of-mass, the normalized rotation rates and speeds of ice floes decrease significantly for larger floe-eddy size ratios. This occurs because the ocean vorticity and velocity at the floe center-of-mass are considerably higher compared to the values averaged over the floe area (figure 2b, d). For both types of ocean quantities, the angle deviation becomes more pronounced as the floe-eddy size ratios increase (figure 2e, f). With larger ratios, the resultant forces from a combination of the Coriolis force and the pressure gradient force due to the sea surface tilt become larger, resulting in a shift of floe trajectories from an outwardly spiral shape to an inwardly spiral shape as the ratios increase. As a result, the angle deviations at $R_f/R_e = 0.5$ are smaller than in the other two cases since the floe trajectories form nearly closed loops. Floes with $R_f/R_e = 1.0$ show positive angle deviations since they have inwardly spiral trajectories.

The motion of a single floe provides insight into the instantaneous response of ice floes to an underlying ocean eddy flow field. Our results demonstrate the importance of floe-eddy size ratios modulating the distribution of forces due to drag, Coriolis, and the pressure gradient on ice floes as they drift over ocean eddy fields.

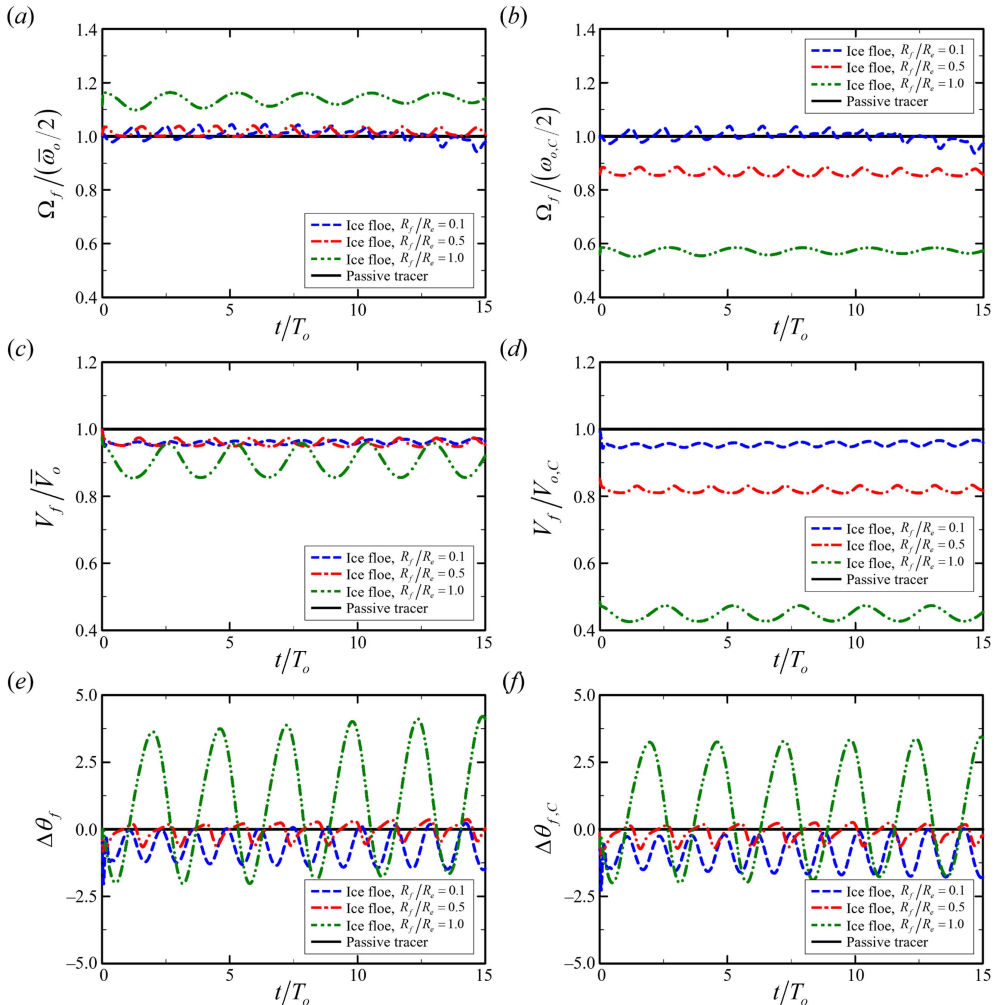


Figure 2: Motions of ice floes with different sizes in a TG vortex field. (a, b) Normalized rotation rates, Ω_f , (c, d) speeds, V_f , and (e, f) angle deviations of ice floes for floe-eddy size ratios of $R_f/R_e = 0.1$ (blue dashed lines), 0.5 (red dot-dashed lines), and 1.0 (green double dot-dashed lines) are compared to the passive tracer case (black solid lines). Floe rotation rates are normalized by the (a) ocean vorticity averaged over the floe area, $\bar{\omega}_o$, and (b) ocean vorticity at the floe center-of-mass, $\omega_{o,C}$. Floe speeds are normalized by (c)

ocean speed averaged over the floe area, \bar{V}_o , and (d) ocean speed at the floe center-of-mass, $V_{o,C}$. Angle deviations are calculated by subtracting the angle of the (e) averaged ocean velocity, $\Delta\theta_f$, and the (f) center-of-mass ocean velocity, $\Delta\theta_{f,C}$, from that of the ice floe velocity. The ice floes are initially released at $r_f/R_e = 0.5$.

3.2. Statistics of ice floe kinematics in an idealized vortex

Based on the statistics of ice floes in a TG vortex field, we derived analytical expressions describing the kinematic link between ice floe rotation and the ocean vorticity underneath. Appendix A outlines the criteria for identifying trapped ice floes. Given the time duration of the simulation and the requirements for floe selection, ice floes with floe-eddy size ratios ranging from 0.05 to 1.4 were considered for further analysis.

We examined ice floes positioned at the center of a TG vortex representing an idealized

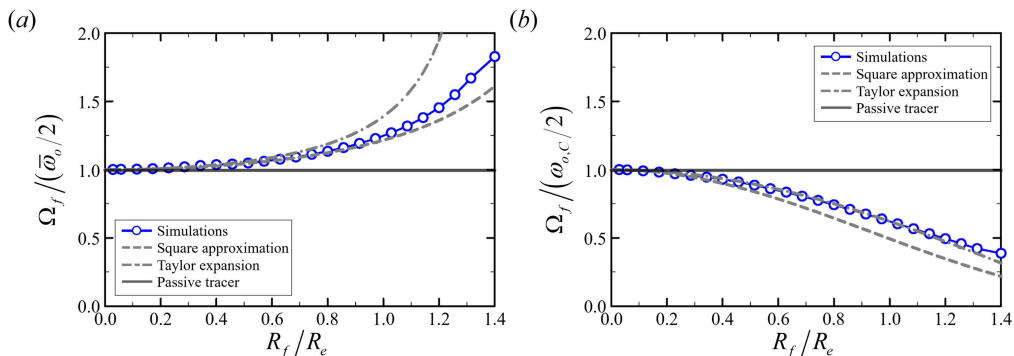


Figure 3: Rotational motion of centered ice floes in a TG vortex field. Ice floe rotation rates, Ω_f , normalized by the (a) ocean vorticity averaged over the floe area, $\bar{\omega}_o$, and the (b) the ocean vorticity at the floe center-of-mass, $\omega_{o,C}$, for different floe-eddy size ratios, R_f/R_e . The simulation results are compared to analytical relations using square-shape approximation (dashed lines) and Taylor series expansion (dashed-dotted lines), and the passive tracer case (solid lines).

scenario (figure 3). In this case, the ice floes are initially released at the center of the vortex, exhibiting a distinct trend in their rotation driven solely by spatial variations in ocean vorticity within the vortex core. The ice floe rotation rate normalized by the ocean vorticity averaged over the floe area shows a monotonic growth with increasing floe-eddy size ratios (figure 3a). This observed rise in rotation rates can be attributed to the gradual decline in local ocean vorticity from the center of a vortex cell toward its periphery. As floe-eddy size ratios increase, the averaged ocean vorticity decreases, increasing normalized rotation rates. In contrast, the rotation rate normalized by the ocean vorticity at the floe center-of-mass decreases for larger floe-eddy size ratios (3b). This behavior can be attributed to the fact that large ice floes rotate at slower rates while the ocean vorticity is maximized at the center-of-mass of the rotating ice floes.

Building upon the physical interpretation of ice floe rotation, we established analytical relations for the normalized rotation rates by balancing the torques acting on the ice floes. In the present analysis, the quadratic drag terms in the angular momentum equation (2.10) are substituted with linear drag, thereby enabling the derivation of explicit relations describing the dependence of the normalized rotation rates on floe-eddy size ratios. We investigated the effect of this substituted parameterization on the rotational relationship using the Rankine vortex, a simplified case for which solutions for both drag parameterizations can be derived. The analytical relation for the normalized rotation rate of ice floes shows minimal sensitivity to the choice of drag parameterization, as detailed in Appendix B, such that a linear drag law was used in deriving an analytical relation.

By introducing a so-called size parameter, $\gamma = R_f/R_e$, we derived an analytical relationship for the normalized rotation rate of an ice floe located at the center of the TG vortex. Near the center of the TG vortex ($2\pi x/L, 2\pi y/L \ll 1$), the ocean surface velocity can be approximated using a Taylor series expansion. In the absence of wind, ice floe rotation is dominated by ice-ocean stress for which the induced equilibrium of torques leads to the relation:

$$\iint_{A^*} \mathbf{r}_f^* \times (\mathbf{u}_f^* - \mathbf{u}_o^*) dA^* = 0. \quad (3.1)$$

Substituting the second-order Taylor series expansion into equation (3.1) yields the following

expression for the ice floe rotation rate normalized by the averaged ocean vorticity:

$$\frac{\Omega_f}{\bar{\omega}_o/2} = \frac{\left[1 - \frac{\pi^2}{8} \left(\frac{\gamma^2}{3}\right) + \frac{\pi^4}{64} \left(\frac{\gamma^4}{48}\right)\right]}{\left[1 - \frac{\pi^2}{8} \left(\frac{\gamma^2}{2}\right) + \frac{\pi^4}{64} \left(\frac{\gamma^4}{24}\right)\right]}, \quad (3.2)$$

where $\gamma = R_f/R_e$. Given that the ocean vorticity at the center-of-mass of the centered floe in the TG vortex is $\omega_{o,C} = 2A\pi^2/L_{TG}^2$, the ice floe rotation rate normalized by the ocean vorticity at the floe center-of-mass can be expressed as:

$$\frac{\Omega_f}{\omega_{o,C}/2} = \left[1 - \frac{\pi^2}{8} \left(\frac{\gamma^2}{3}\right) + \frac{\pi^4}{64} \left(\frac{\gamma^4}{48}\right)\right]. \quad (3.3)$$

Equation (3.2) is in good agreement with the simulation results for the rotation rates normalized by the averaged ocean vorticity provided $R_f/R_e \leq 0.7$ (figure 3a). In this range, the Taylor series approximation effectively restores the original functions. However, we observed noticeable deviations in the normalized rotation rate when the ice floe size exceeded the eddy size due to limitations of the Taylor series expansion near the edge of the vortex cell. Equation (3.3) aligns well with simulation results for the rotation rate normalized by the ocean vorticity at the floe center-of-mass for different floe-eddy size ratios because the ocean vorticity remains constant (figure 3b).

We derived another analytical relation for the normalized rotation rate of the centered ice floe by approximating the floe shape as a square with the same characteristic length scale. With the equilibrium condition for ice-ocean stress torques, the analytical relation can be expressed as:

$$\frac{\Omega_f}{\bar{\omega}_o/2} = \frac{12}{\pi^2\gamma} \left[1 - \frac{\pi\gamma}{2} \cot\left(\frac{\pi\gamma}{2}\right)\right]. \quad (3.4)$$

We positioned square-shaped floes centered with respect to the origin. This simplification allows for the direct use of trigonometric functions. As a result, the ice floe rotation rate normalized by the ocean vorticity at the floe center of mass can be written as:

$$\frac{\Omega_f}{\omega_{o,C}/2} = \frac{12}{\pi^2\gamma} \left[\frac{\sin\left(\frac{\pi\gamma}{2}\right)}{\frac{\pi\gamma}{2}}\right]^2 \left[1 - \frac{\pi\gamma}{2} \cot\left(\frac{\pi\gamma}{2}\right)\right]. \quad (3.5)$$

Equation (3.4) closely matches the simulation results for the rotation rates normalized by the averaged ocean vorticity because it incorporates trigonometric functions fully in the solution (figure 3a). However, equation (3.5) deviates from the simulation results for the rotation rates normalized by the center-of-mass ocean vorticity due to the square-shape approximation (figure 3b). It is worth noting that, for the centered ice floes, the derived analytical relations (3.2)–(3.5) are functions solely of the floe-eddy size ratios.

We also examined a more realistic scenario of an ice floe being positioned off-center with respect to the TG vortex cell. We conducted simulations with over 2,000 randomly distributed ice floes for each floe-eddy size ratio. While centered ice floes remain at the vortex center, off-centered ice floes have the potential to drift away, depending on their radial positions. For the present analysis, only trapped ice floes were considered.

The normalized rotation rates of off-centered floes are dependent on the position of the floes relative to the vortex core. Therefore, to analyze this case, we computed probability density functions (PDF) over all floe positions for each bin of floe-eddy size ratios (figure

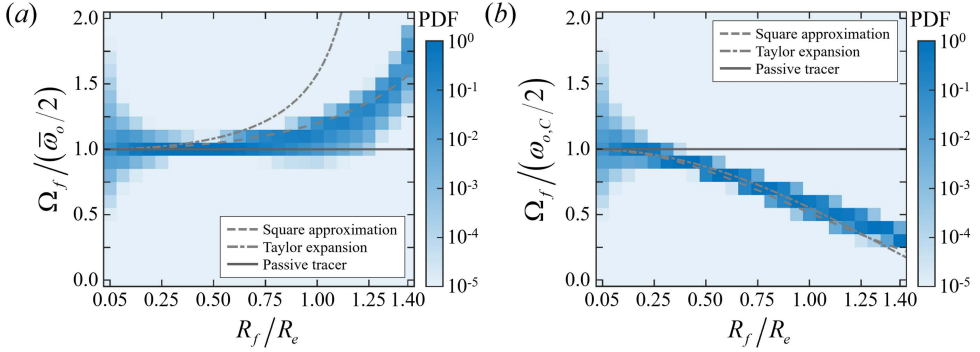


Figure 4: Rotational motion of off-centered ice floes in a TG vortex field. PDF of ice floe rotation rates, Ω_f , normalized by the (a) ocean vorticity averaged over the floe area, $\bar{\omega}_o$, and the (b) ocean vorticity at the floe center-of-mass, $\omega_{o,C}$, for different floe-eddy size ratios. The simulation results are compared to analytical relations using square-shape approximation (dashed lines) and Taylor series expansion (dashed-dotted lines), and the passive tracer case (solid lines).

4). As discussed in the single floe analyses (§3.2), the observed variability arises from floe inertia, causing a delay in ice floe response to changes in the underlying ocean eddy field. This delay results in a discrepancy between the rotation of the ice floes and the underlying ocean eddies. Considering ice floe rotation rates normalized by the averaged ocean vorticity, ice floes behave as passive tracers provided $R_f/R_e \leq 0.7$ (figure 4a). However, as the floe-eddy size ratio increases and approaches 1.4, the peaks in the normalized rotation rates shift to greater values, reaching approximately 1.8, similar to the case of centered ice floes (figure 3a). Around $R_f/R_e \approx 0.5$, the distribution narrows and exhibits higher peaks, suggesting that a solid body rotation approximation accurately captures floe motion within this range of floe-eddy size ratios. This behavior can be attributed to the ice floe area filtering out ice floe-ocean stress, thereby reducing ice floe responsiveness to any variability within the vortex cell. As floe-eddy size ratios increase, excessive filtering of ocean information over the ice floe diminishes sensitivity to underlying ocean characteristics, resulting in a broadening of the PDF. For ice floe rotation rates normalized by the ocean vorticity at the floe center-of-mass, ice floes behave as passive tracers when $R_f/R_e \leq 0.25$. The peaks of the PDF shift to smaller values as the size ratios increase, reaching approximately 0.25 at $R_f/R_e = 1.4$ (figure 4b). Similar to the behavior observed for averaged ocean vorticity, the distributions are more dispersed for small floes, while clear peaks are evident for $R_f/R_e \geq 0.25$, as the center-of-mass ocean vorticity for larger floes tends to exceed the area-averaged vorticity.

Following the same approach as for centered ice floes, we derived analytical relations for the off-centered floes. By employing the Taylor series expansion, the analytical relations for the ice floe rotation rate normalized by the averaged ocean vorticity can be derived as:

$$\frac{\Omega_f}{\bar{\omega}_o/2} = \frac{\left\{ 1 - \frac{\pi^2}{8} \left[\frac{\gamma^2}{3} + \left(\frac{r_f}{R_e} \right)^2 \right] + \frac{\pi^4}{64} \left[\frac{\gamma^4}{48} + \frac{\gamma^2}{6} \left(\frac{r_f}{R_e} \right)^2 + \left(\frac{x_f}{R_e} \right)^2 \left(\frac{y_f}{R_e} \right)^2 \right] \right\}}{\left\{ 1 - \frac{\pi^2}{8} \left[\frac{\gamma^2}{2} + \left(\frac{r_f}{R_e} \right)^2 \right] + \frac{\pi^4}{64} \left[\frac{\gamma^4}{24} + \frac{\gamma^2}{4} \left(\frac{r_f}{R_e} \right)^2 + \left(\frac{x_f}{R_e} \right)^2 \left(\frac{y_f}{R_e} \right)^2 \right] \right\}}, \quad (3.6)$$

where x_f and y_f are the horizontal and vertical Cartesian coordinates of the floe center of mass, respectively, and $r_f = \sqrt{x_f^2 + y_f^2}$ is its radial position. Similarly, the ice floe rotation

rate normalized by the center-of-mass ocean vorticity can be then expressed as:

$$\frac{\Omega_f}{\omega_{o,c}/2} = \frac{\left\{ 1 - \frac{\pi^2}{8} \left[\frac{\gamma^2}{3} + \left(\frac{r_f}{R_e} \right)^2 \right] + \frac{\pi^4}{64} \left[\frac{\gamma^4}{48} + \frac{\gamma^2}{6} \left(\frac{r_f}{R_e} \right)^2 + \left(\frac{x_f}{R_e} \right)^2 \left(\frac{y_f}{R_e} \right)^2 \right] \right\}}{\left[1 - \frac{\pi^2}{8} \left(\frac{r_f}{R_e} \right)^2 + \frac{\pi^4}{64} \left(\frac{x_f}{R_e} \right)^2 \left(\frac{y_f}{R_e} \right)^2 \right]}. \quad (3.7)$$

In contrast to the centered ice floe cases, relations (3.6) and (3.7) not only depend on the floe-eddy size ratio, but also on the radial positions of the ice floes. Therefore, the normalized rotation rates were averaged over all r_f values for each of the floe-eddy size ratio bins. As $r_f \rightarrow 0$, the analytical relations for the off-centered floes (equations 3.6 and 3.7) converge to the relations for the centered floes (equations 3.2 and 3.3). Equation (3.6) is in good agreement with the PDF peaks for small floe-eddy size ratios (figure 4a). Their differences become evident around $R_f/R_e \approx 0.5$ and become more pronounced for larger size ratios due to the issues of the Taylor series expansion near the cell edges. Conversely, equation (3.7) closely aligns with the PDF peaks of ice floe rotation rates normalized by the center-of-mass vorticity for most floe-eddy size ratios (figure 4b).

The square-shape approximation for off-centered floes yields the same analytical relations as for centered floes. Thus, equations 3.4 and 3.5 are also used to describe the rotation rates of off-centered floes. These equations match the PDF peaks over a wide range of floe-eddy size ratios and only show minor deviations at ratios around $R_f/R_e = 1.4$ (figures 4a and 4b). Overall, the square-shape approximation provides accurate estimates of the PDF peak compared to the Taylor series approximation.

The PDFs of normalized ice floe speeds and floe-ocean angle deviations depend on the floe-eddy size ratios (figure 5), corresponding to the results of single floe analyses depicted in figure 2. For the ice floe speed normalized by the ocean speed averaged over the floe area, the PDF peaks at unity ($V_f/\bar{V}_o = 1$), resembling the behavior of a passive tracer (figure 5a). As the floe-eddy size ratio increases and approaches 1.4, the normalized speed at the PDF peaks gradually decreases to $V_f/\bar{V}_o = 0.75$. In contrast to the ice floe rotation rate results, the PDFs of normalized floe speeds for small-sized floes exhibit narrow distributions. This trend can be attributed to the fact that the Coriolis force and the pressure gradient force due to the sea surface tilt depend on the velocity difference, $\Delta \mathbf{u}_f = \bar{\mathbf{u}}_o - \mathbf{u}_f$, while the torque generated by these forces depends solely on ocean velocity, $\bar{\mathbf{u}}_o$, with no contribution from the Coriolis force. As a result, floe speed is less responsive to changes in ocean speed. This is reflected in the third term of equation (2.9), which is derived using the geostrophic balance between the pressure gradient force due to sea surface tilt and the Coriolis force.

Overall, the ocean speed at the floe center-of-mass is greater than the ocean speed averaged over the floe area. The peaks of the PDF for the floe speed normalized by the center-of-mass ocean speed decrease to 0.25 as the floe-eddy size ratio increases to 1.4 (figure 5b). It is useful to note that the velocity difference between the ice floe and the underlying ocean remains relatively constant across different floe-eddy size ratios, such that $|\Delta \mathbf{u}_f| \approx C_0$, where C_0 denotes a constant. This value can be derived by equating the magnitude of the ice floe-ocean stress (the first term on the right-hand side of equation 2.9) to a combination of the Coriolis force on the ice floe and the pressure gradient force due to the sea surface tilt (the third term on the right-hand side of equation 2.9) under torque equilibrium, as follows: $|\Delta \mathbf{u}_f|^2/H_{f,o}^* \sim |\Delta \mathbf{u}_f^*|/Ro$. Then, the floe speed normalized by the averaged ocean velocity can

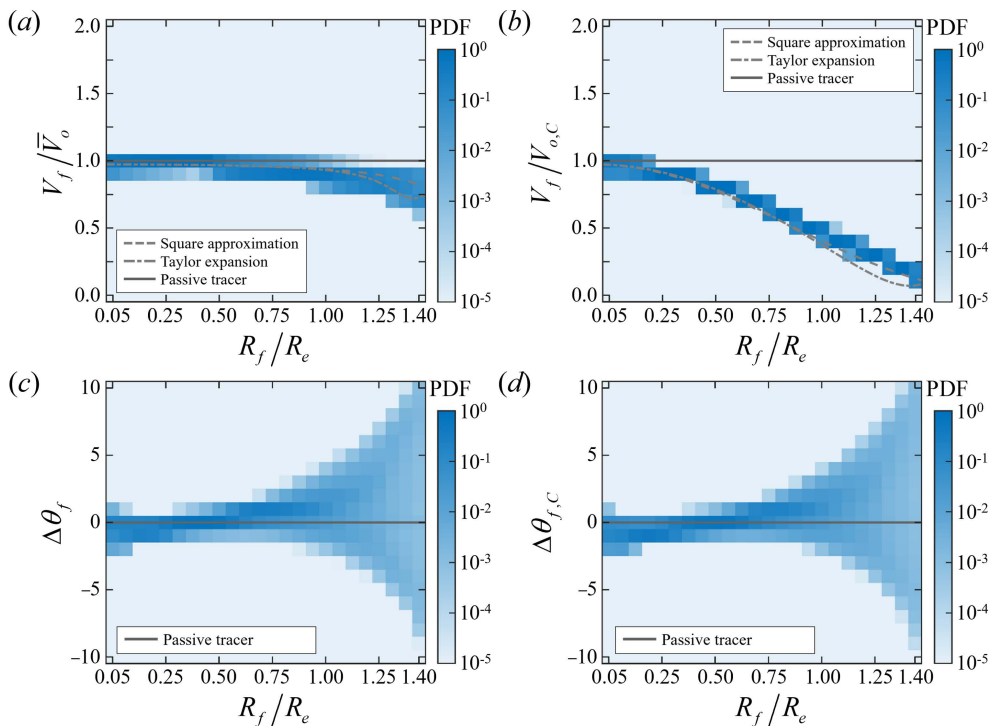


Figure 5: Translational motion of off-centered ice floes in a TG vortex field. PDF of ice floe speed, V_f , normalized by the (a) ocean speed averaged over the floe area, \bar{V}_o , and the (b) ocean speed at the floe center-of-mass, $V_{o,C}$, and (c and d) angle deviations. For these last quantities, ice and ocean velocity angles are calculated using the direction of each velocity vector with respect to the positive x -axis, measured in the counter-clockwise direction. Then, deviations are computed by subtracting the angle of (c) the averaged ocean velocity, $\Delta\theta_f$, and the (d) center-of-mass ocean velocity, $\Delta\theta_{f,C}$, from that of the ice floe velocity, for different floe-eddy size ratios. The simulation results are compared to analytical relations using square-shape approximation (dashed lines) and Taylor series expansion (dashed-dotted lines), and the passive tracer case (solid lines).

be expressed as:

$$\frac{V_f}{\bar{V}_o} \approx 1 - \frac{C_0}{\bar{V}_o}, \quad (3.8)$$

implying that for lower averaged ocean speeds as in the case of larger floes, there is a reduction in normalized floe speeds.

Similar to equations (3.6)–(3.7), the analytical relation for ice floe speed normalized by the ocean speed averaged over the floe area and by the ocean speed at the floe center-of-mass can be derived using the Taylor series expansion and the square-shape approximation. In relation (3.8), the averaged ocean speed can be approximated using a Taylor series expansion as follows:

$$\bar{V}_o = \left(\frac{\pi}{2}\right)^2 \left(\frac{A_{TG}}{R_e}\right) \left(\frac{r_f}{R_e}\right) M_o, \quad (3.9)$$

where M_o is given by

$$M_o = 1 - \frac{1}{12} \left(\frac{\pi}{2}\right)^2 \left\{ 3\gamma^2 + 2 \left[\left(\frac{x_f}{R_e}\right)^2 + 3 \left(\frac{y_f}{R_e}\right)^2 \right] \right\} \\ + \frac{1}{96} \left(\frac{\pi}{2}\right)^4 \left\{ \gamma^4 + 2\gamma^2 \left[\left(\frac{x_f}{R_e}\right)^2 + 3 \left(\frac{y_f}{R_e}\right)^2 \right] + 8 \left(\frac{x_f}{R_e}\right)^2 \left(\frac{y_f}{R_e}\right)^2 \right\}. \quad (3.10)$$

Similarly, the ice floe speed normalized by the center-of-mass ocean speed can be expressed using the averaged ocean speed as follows:

$$\frac{V_f}{V_{o,C}} = \left(1 - \frac{C_0}{\bar{V}_o}\right) \left(\frac{\bar{V}_o}{V_{o,C}}\right). \quad (3.11)$$

The center-of-mass ocean speed can also be approximated using the Taylor series expansion:

$$V_{o,C} = \left(\frac{\pi}{2}\right)^2 \left(\frac{ATG}{R_e}\right) \left(\frac{r_f}{R_e}\right) M_{o,C}, \quad (3.12)$$

where $M_{o,C}$ is given by

$$M_{o,C} = 1 - \frac{2}{3} \left(\frac{\pi}{2}\right)^2 \left(\frac{r_f}{R_e}\right)^2 \left[1 + \left(\frac{x_f}{r_f}\right)^2 \left(\frac{y_f}{r_f}\right)^2 \right] \left[1 + \frac{1}{6} \left(\frac{\pi}{2}\right)^4 \left(\frac{x_f}{R_e}\right)^2 \left(\frac{y_f}{R_e}\right)^2 \right] \\ - \frac{1}{9} \left(\frac{\pi}{2}\right)^4 \left(\frac{r_f}{R_e}\right)^4 \left[1 + \frac{21}{4} \left(\frac{x_f}{r_f}\right)^2 \left(\frac{y_f}{r_f}\right)^2 + \frac{1}{4} \left(\frac{\pi}{2}\right)^4 \left(\frac{r_f}{R_e}\right)^4 \left(\frac{x_f}{r_f}\right)^4 \left(\frac{y_f}{r_f}\right)^4 \right]. \quad (3.13)$$

Note that for comparison with the simulation results, the normalized floe speeds in the analytical relations were averaged over all r_f values for each bin of floe-eddy size ratios. Similarly, using the square-shape approximation, the averaged ocean speeds can be approximated as the following:

$$\bar{V}_o = \left(\frac{\pi}{2}\right) \left(\frac{ATG}{R_e}\right) \left[\sin\left(\frac{\pi R_f}{2 R_e}\right) / \left(\frac{\pi R_f}{2 R_e}\right) \right]^2 \\ \left[\cos^2\left(\frac{\pi x_f}{2 R_e}\right) \sin^2\left(\frac{\pi y_f}{2 R_e}\right) + \sin^2\left(\frac{\pi x_f}{2 R_e}\right) \cos^2\left(\frac{\pi y_f}{2 R_e}\right) \right]^{1/2}. \quad (3.14)$$

The center-of-mass ocean speed can also be obtained as:

$$V_{o,C} = \left(\frac{\pi}{2}\right) \left(\frac{ATG}{R_e}\right) \left[\cos^2\left(\frac{\pi x_f}{2 R_e}\right) \sin^2\left(\frac{\pi y_f}{2 R_e}\right) + \sin^2\left(\frac{\pi x_f}{2 R_e}\right) \cos^2\left(\frac{\pi y_f}{2 R_e}\right) \right]^{1/2}. \quad (3.15)$$

The analytical relation using the square-shape approximation (equations 3.14 and 3.15) shows good agreement with the peaks of the normalized speeds, while the analytical relation using the Taylor series expansion (equations 3.9 and 3.12) exhibits deviations for $R_f/R_e \geq 1$ (figures 5a and 5b). The constant $C_0 = 0.15$ was chosen, producing the best-fit to the PDF peaks. Note that as $r_f \rightarrow 0$, the analytical relations for the normalized floe speed (equations 3.8 and 3.11) converge to the centered floe case as expected.

The PDFs of the angle deviation between ice floe velocity and ocean velocity are also contingent on the floe-eddy size ratio (figures 5c and 5d). As discussed in the single floe analysis (figure 2), the velocity of larger floes exhibits greater deviations from ocean velocity, including the averaged ocean velocity and the center-of-mass velocity, thus resulting in more

dispersed distributions for larger floe-eddy size ratios. While the vectors of the averaged ocean velocity and the center-of-mass ocean velocity differ slightly in magnitude, their orientations are the same. This observation can be readily confirmed using the square-shape approximation, as follows:

$$\tan \bar{\theta}_o = -\tan \left(\frac{\pi x_f}{2 R_e} \right) \Big/ \tan \left(\frac{\pi y_f}{2 R_e} \right) = \tan \theta_{o,C}, \quad (3.16)$$

indicating that the angle of the averaged ocean velocity is equal to the angle of the center-of-mass ocean velocity.

In addition to calculating ocean velocity and vorticity beneath single ice floes, we can also compute local ocean vorticity from Green's theorem by using ice floe trajectory information. Passive tracers trapped in an eddy exhibit closed-loop trajectories. In this case, we can estimate the averaged ocean vorticity of the region enclosed by the trajectory as $\tilde{\omega}_o = \oint \mathbf{u}_{tr} \cdot d\mathbf{S}_{tr}$, where \mathbf{u}_{tr} is the tracer velocity, \mathbf{S}_{tr} is the tracer trajectory, and \sim denotes the averaged quantity over the closed region. Here, since $\mathbf{u}_{tr} = \mathbf{u}_o$, the true ocean vorticity, $\tilde{\omega}_o$, can be obtained. Similarly, trapped ice floes have been observed to form nearly closed-loop patterns, with the endpoints slightly offset from the starting points. However, as previously discussed, the velocity of ice floes corresponds to the filtered ocean velocity over the floe area but is not exactly the same. As a result, any averaged ocean vorticity estimate within a trajectory-enclosed region, $\tilde{\omega}_f$, does not match the true averaged ocean vorticity of the same region, $\tilde{\omega}_f \neq \tilde{\omega}_o$. Nonetheless, their ratios can be approximated using the ice floe and underlying ocean velocities as:

$$\frac{\tilde{\omega}_f}{\tilde{\omega}_o} = \frac{\oint \mathbf{u}_f \cdot d\mathbf{S}_f}{\oint \mathbf{u}_{o,C} \cdot d\mathbf{S}_f} \approx \frac{V_f}{V_{o,C}}, \quad (3.17)$$

where $\mathbf{u}_{o,C}$ is the ocean velocity at the floe center of mass and \mathbf{S}_f is the ice floe trajectory.

Floe trajectories are not perfectly closed, with just a short segment between the start and endpoints. Hence, the line integration in equation 3.17 is conducted from the first to the last points. The true averaged ocean vorticity can be calculated by integrating the center-of-mass ocean velocity along the floe trajectory. The ratio of the ocean vorticity estimate based on ice floe velocity to the true ocean vorticity, $\tilde{\omega}_f/\tilde{\omega}_o$, can be approximated by the normalized ice floe speed, $V_f/V_{o,C}$ (equation 3.17).

The PDFs of the ratio between the ocean vorticity estimate and the true ocean vorticity depend on floe-eddy size ratios (figure 6). The floe speed normalized by the center-of-mass ocean speed significantly decreases for larger floe-eddy size ratios (figure 5b), resulting in smaller vorticity ratios. Furthermore, the peaks of the PDF for most floe-eddy size ratios align with the analytical relation for normalized floe speed using the square-shape approximation (equations 3.11, 3.14, and 3.15). The relation using the Taylor series expansion (equations 3.11–3.13) is in good agreement with the PDF peaks for $R_f/R_e \leq 0.75$, showing a discrepancy for larger ratios due to the coverage limit of the Taylor series expansion near the edge of the vortex cell.

3.3. Statistics of ice floe kinematics in a QG flow field

We performed simulations of ice floes in a QG flow field to apply the derived analytical relations to a more realistic ocean eddy field (figure 7a). Passive tracers were released into the flow field, and ocean vorticity was interpolated to the Lagrangian tracer positions. Then, a LAVD-based eddy detection method (Haller *et al.* 2016) was used to identify the boundaries of eddies by searching for the outermost closed contour of the LAVD, which indicates local rotation relative to mean rotation. The LAVD was computed by averaging the vorticity

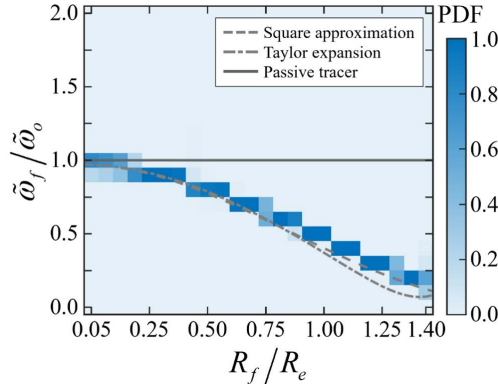


Figure 6: Averaged ocean vorticity estimates from ice floe trajectories in a TG vortex field. PDF of ratios between the averaged ocean vorticity of the region enclosed by ice floe trajectories, $\tilde{\omega}_f$, and the true averaged ocean vorticity of the region, $\tilde{\omega}_o$, for different floe-eddy size ratios. The simulation results are compared to analytical relations using the square-shape approximation (dashed line) and Taylor series expansion (dashed-dotted line), and the passive tracer case (solid line).

deviation along the Lagrangian tracer trajectory as follows:

$$\text{LAVD}(x_0, y_0) = \omega'_o [X(x_0, y_0), Y(x_0, y_0)], \quad (3.18)$$

where (X, Y) are the coordinates of tracers with an initial position of (x_0, y_0) , and ω'_o is the vorticity deviation from the spatial average over the whole domain. Given that the ocean field is time-independent in the present study, the time component is not considered in equation (3.18). A total of 70 eddies were identified in the QG flow field (figure 7a); their morphologies become more apparent in the LAVD field (figure 7b). Note that while the LAVD have been widely used to capture vorticity-dominated structures in atmospheric and oceanic flows, it has proven ineffective in capturing rapidly evolving vortices or highly transient flow fields (Aksamit *et al.* 2024).

We selected four varying-size representative eddy cases to examine the kinematic link between drifting ice floes and the underlying flow field (figures 7c–f). To this end, we randomly released over 2,000 ice floes near each eddy, identifying floes trapped within vortex cores (Appendix A). Ice floes released near the eddy boundary exhibited nearly closed-loop trajectories resembling the shapes of the eddies (figures 7c–f). Hence, the trajectories of individual trapped ice floes provide a direct estimate of local eddy length scales, whereby the size of the largest enclosed region by ice floe trajectories, $R_{traj} = \sqrt{A_{traj}/\pi}$, was chosen as a trajectory-derived length scale for each local eddy. Here, A_{traj} is the area of the largest enclosed region by ice floe trajectories. This length scale closely matches the eddy size in the TG vortex.

In QG eddies, ice floes simultaneously covering both the inside and outside regions of an eddy often become entrapped by the eddy, resulting in minor discrepancies between eddy size and trajectory-derived length scales. These differences arise due to variations in vorticity and velocity distributions among different QG eddies, leading to diverse trajectory shapes and trajectory-derived length scales. In the selected QG eddies, R_f/R_{traj} range from 0.05 to 1.25. Beyond these ranges, ice floes generally remain translating near the eddies or drift away from them over the simulation period.

We investigated the rotational relationship between isolated ice floes and the underlying local eddies for the four eddies marked in figure 7. Despite variations in eddy size and

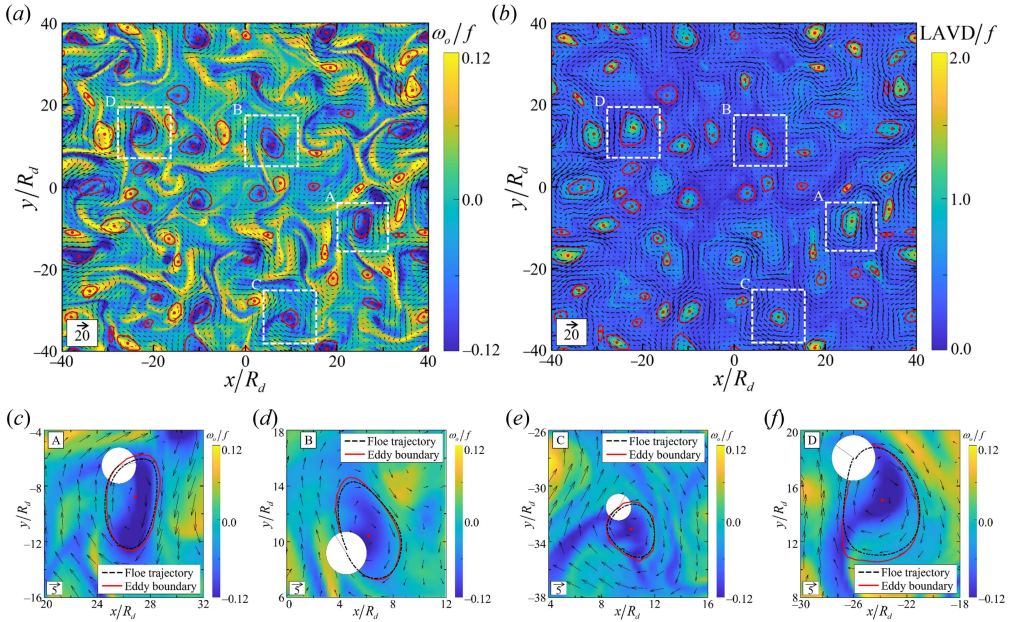


Figure 7: Motion of ice floes in a QG flow field. Boundaries (red lines) and centers (red dots) of the detected eddies are shown in the field of (a) ocean vorticity and (b) LAVD normalized by the Coriolis parameter f . (c–f) Representative cases of trajectories (black dashed lines) of isolated ice floes within local eddies marked as A to D with white dashed boxes in the QG and LAVD flow fields, respectively. The color and arrows in the figure correspond to the magnitude of the normalized vorticity and LAVD and the magnitude and direction of the velocity at a given location, respectively. The floes (white circle) are positioned at the endpoint of their trajectories.

shape, the normalized rotation rates of ice floes showed similar qualitative and quantitative trends to those in the idealized vortex cases (figure 8). Notably, the PDFs of ice floe rotation rates, normalized by the ocean vorticity averaged over the floe area, peak at unity when $R_f/R_{traj} \leq 0.5$ for all four cases (figure 8). Note how the distributions of the normalized floe rotation rates in the QG eddy cases are more dispersed than in the TG vortex cases. We attribute this discrepancy to the highly nonlinear, deformed eddies dominant in the QG flow field. The PDF peaks become more pronounced in the QG cases as the floe size approaches half of the trajectory-derived length scale ($R_f/R_{traj} = 0.5$). The peaks shift toward 1.5 as R_f/R_{traj} hits 1.25. Analytical relations derived for the TG vortex effectively characterize this behavior. The relation from the Taylor series expansion (equation 3.6) aligns with PDF peaks for smaller R_f/R_{traj} , while the relation from the square-shape approximation (equation 3.4) agrees well with the peaks across most size ratios.

The PDFs of ice floe rotation rates normalized by the ocean vorticity at the floe center of mass exhibit similar qualitative behaviors compared to the idealized vortex case (figure 9). As R_f/R_{traj} increases to 1.25, the PDF peaks decrease to 0.25, consistent with the TG vortex cases (figure 4b). However, analytical relations (3.5) and (3.7), derived for the TG vortex, exhibit discrepancies with the PDF peaks due to differences in the eddy structures of the flow fields. Vorticities near the center of QG eddies exhibit smaller spatial gradients compared to the TG vortex, leading to smaller normalized rotation rates in the QG eddy cases. In addition, the center-of-mass ocean vorticity changes abruptly across regions, contrasting with the averaged ocean vorticity, such that the rotation rates normalized by the center-

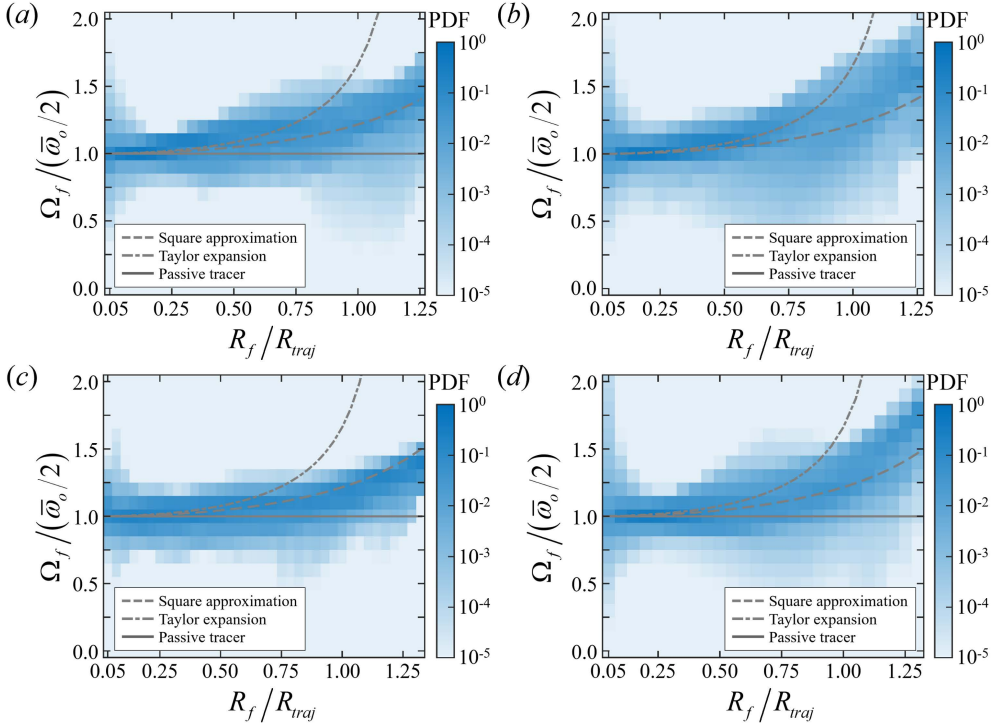


Figure 8: Rotational motion of isolated ice floes in local QG eddies. (a–d) PDF of ice floe rotation rates, Ω_f , normalized by the averaged ocean vorticity over the floe area, $\bar{\omega}_o$, for different ratios between floe size and trajectory-derived length scale, R_f/R_{traj} , in local eddies marked as A to D with white dashed boxes in a QG flow field, respectively. The simulation results are compared to analytical solutions using square-shape approximation (dashed line), Taylor series expansion (dashed-dotted line), and the passive tracer case (solid line).

of-mass ocean vorticity show more discrepancies with the TG vortex cases and analytical relations derived for them.

The ocean vorticity estimate of the region enclosed by ice floe trajectories in QG eddies exhibits similar trends to the estimate in the TG vortex (figure 10). The PDFs of the ratio between the ocean vorticity estimate and true ocean vorticity reach their peaks at unity. However, these peaks decrease to 0.25 for larger R_f/R_{traj} , reaching up to 1.25. This trend is likely due to a greater discrepancy between the averaged ice floe velocity and the ocean velocity at the floe center of mass in QG eddies. Overall, analytical relation (3.17) captures the qualitative behavior of the PDF peaks, albeit with minor quantitative discrepancies observed for certain R_f/R_{traj} .

The observed ice floe motions and their analytical relations to the ocean, derived from the idealized eddies, offer insights into the rotational relationship between ice floes and local eddies in the QG flow field. These findings demonstrate the potential applicability of these derived relations to analyze ocean eddies and estimate their vorticity using ice floes. The complexity in the QG case stems from how each eddy exhibits a unique structure, velocity, and vorticity distribution, as illustrated in figure 7. These fundamental differences between the TG vortex and QG eddies limit the direct application of these relationships to QG fields. Nonetheless, further investigation, including analyzing the effects of deformed eddy configurations and different vortex types, holds promise for developing a comprehensive

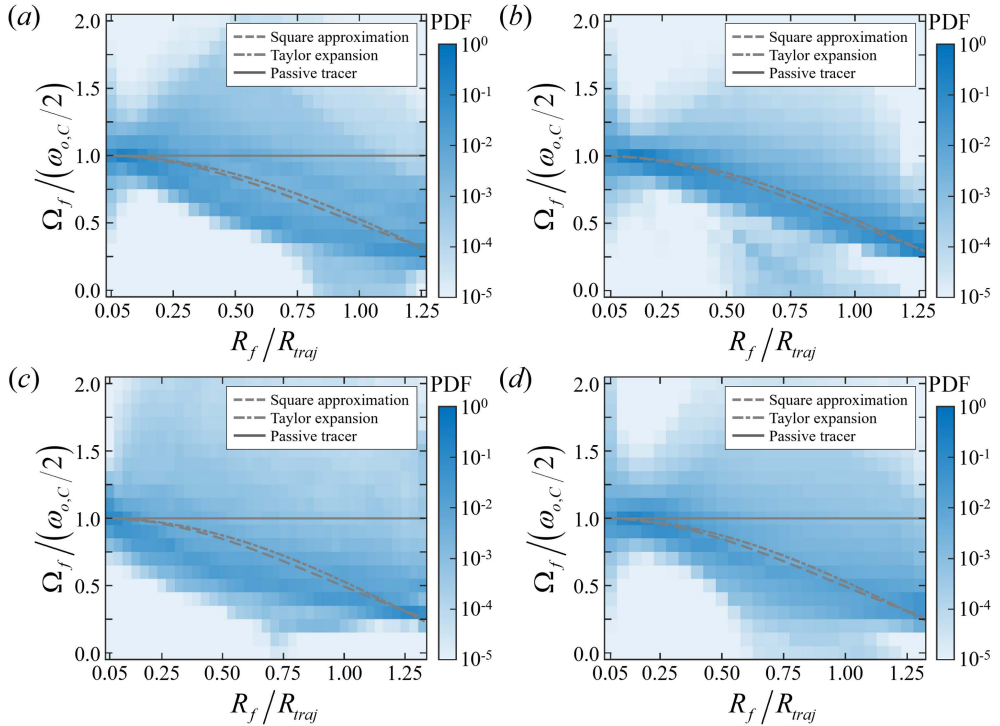


Figure 9: Rotational motion of isolated ice floes in local QG eddies. (a–d) PDF of ice floe rotation rates, Ω_f , normalized by the ocean vorticity at the floe center of mass, $\omega_{o,C}$, for different ratios between floe size and trajectory-derived length scale in local eddies marked as A to D with white dashed boxes in a QG flow field, respectively. The simulation results are compared to analytical solutions using square-shape approximation (dashed line), Taylor series expansion (dashed-dotted line), and the passive tracer case (solid line).

framework to characterize the ocean eddy field from ice floe satellite remote sensing observations.

4. Discussion and further analyses

Following the analysis with idealized free-drifting ice floes, we investigated additional relevant factors influencing the link between ice floe rotation and the vorticity of underlying ocean eddies. Specifically, we discuss the effects of ice floe thickness, atmospheric winds, and floe-floe collisions, corresponding to specific sea ice concentrations, on the rotational relationship between ice floes and the TG vortex.

4.1. Effects of ice floe thickness on ice floe kinematics

The motion of ice floes is affected by their inertia, which is closely linked to their thickness. Thicker ice floes inherently possess greater inertia than thinner floes, leading to increased discrepancies between ice floe motions and the underlying ocean kinematics. Observations of ice floe thickness in the BG MIZ are limited (Haas & Druckenmiller 2009), but estimates typically fall within the order of $O(0.1)$ m, especially during the spring-to-summer season (Manucharyan *et al.* 2022a). To assess the influence of thickness on our results, we performed additional simulations considering floes with ice floe thicknesses ranging from 0.1 m to 1 m, corresponding to $H_{f,o}^* = 1.0 \times 10^{-3} - 1.0 \times 10^{-2}$, for three different floe-eddy size ratios.

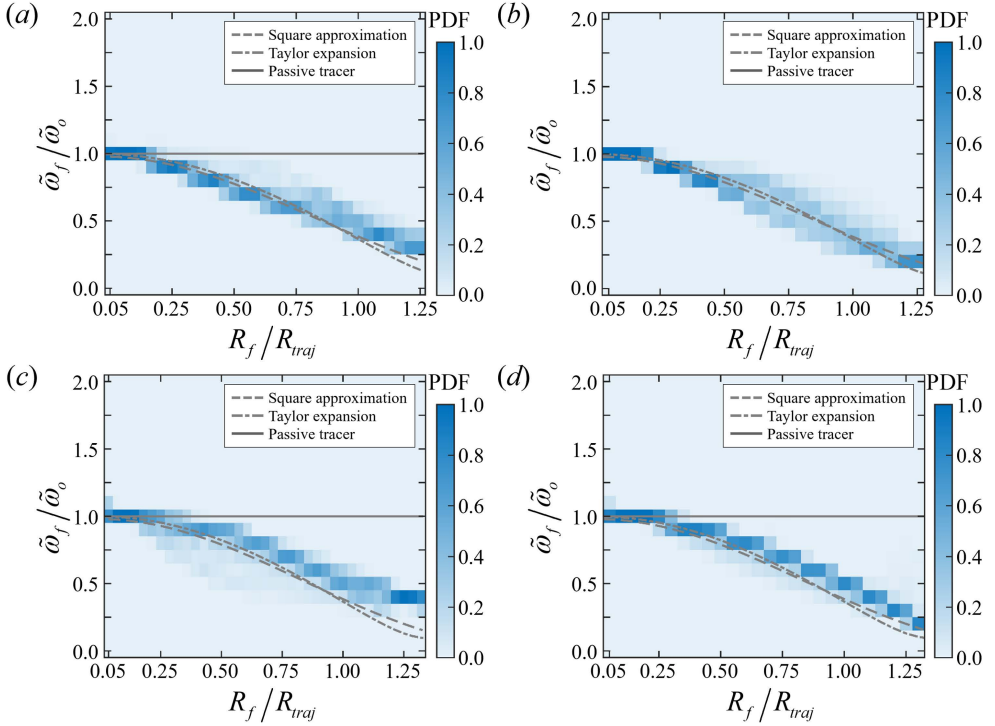


Figure 10: Averaged ocean vorticity estimate using ice floe trajectories in local QG eddies.

(a–d) PDF of ratios between averaged ocean vorticity of the floe trajectory-enclosed region, $\tilde{\omega}_f$, normalized by true averaged ocean vorticity of the same region, $\tilde{\omega}_o$, for different ratios between floe size and trajectory-derived length scale in local eddies marked as A to D with white dashed boxes in a QG flow field, respectively. The simulation results are compared to analytical solutions using square-shape approximation (dashed line), Taylor series expansion (dashed-dotted line), and the passive tracer case (solid line).

We examined the PDFs of normalized ice floe rotation rates and the trajectory-derived ocean vorticity estimates.

The sensitivity of the rotational relationship to ice floe thickness depends on the floe-eddy size ratio, with smaller ice floes being the most responsive to changes in ice floe thickness (figure 11). For $R_f/R_e = 0.1$, the PDF of the normalized rotation rates consistently peaks at unity (figures 11a, b). However, as ice floes become thicker, their inertia increases, leading to greater deviations in their rotation from the ocean rotation. As a result, the peaks gradually diminish, and the distributions become more dispersed. In addition, thicker ice floes tend to follow a more pronounced spiral trajectory, resulting in skewed distributions toward larger normalized rotation rates. Similarly, the PDFs of the ratio between averaged ocean vorticity estimates of the trajectory-enclosed region and true averaged ocean vorticity peak at unity (figure 11c). However, for thicker ice floes, the peaks gradually decrease, and the distributions become more dispersed and skewed toward lower ratios.

As the floe-eddy size ratio increases, the effect of ice floe thickness on the rotational relationship becomes relatively minor (figures 11d–i). Specifically, at $R_f/R_e = 0.5$, thicker ice floes exhibit more dispersed distributions for the rotation rate normalized by the averaged ocean vorticity, skewed toward larger values (figure 11d). In contrast, these floes show negligible changes in the rotation rate normalized by the center-of-mass vorticity and in the averaged ocean vorticity estimates normalized by the true ocean vorticity (figures 11e, f). At

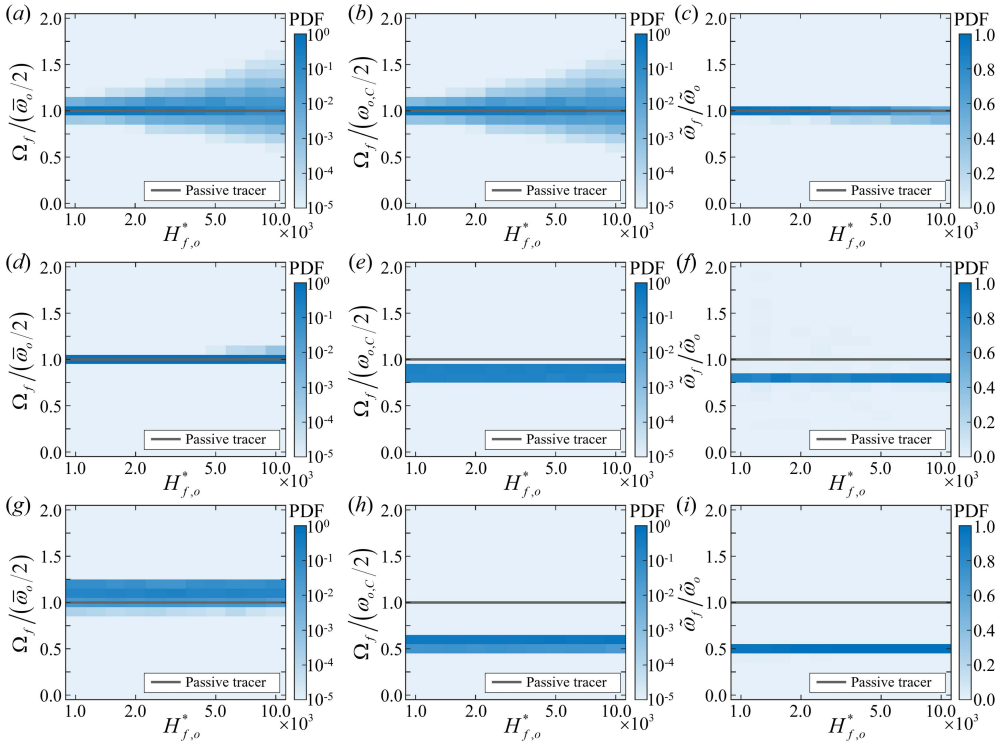


Figure 11: Motion of isolated ice floes with different thicknesses in a TG vortex. PDF of ice floe rotation rate, Ω_f , normalized by the (a, d, g) averaged ocean vorticity over the floe area, $\bar{\omega}_o$, and the (b, e, h) ocean vorticity at the floe center-of-mass, $\omega_{o,C}$. and of (g, h, i) ratio between estimated ocean vorticity averaged over the trajectory-enclosed region, $\tilde{\omega}_f$, and true ocean vorticity of the same region, ω_o , for different floe-eddy size ratios, $R_f/R_e = (a, b, c) 0.1$, (d, e, f) 0.5. and (g, h, i) 1.0.

$R_f/R_e = 1.0$, the PDFs become more dispersed compared to floes with $R_f/R_e = 0.5$ (figures 11g – i), as discussed in §3. However, thicker ice floes exhibit nearly identical distributions to thinner ice floes, indicating negligible effects of ice floe thickness. Overall, thicker ice floes tend to follow more pronounced spiral trajectories due to their increased inertia. Nevertheless, these larger floes are less sensitive to changes in ocean information over the floe area, as this information is filtered out, resulting in minor changes in the rotational relationship between ice floes and the underlying ocean.

4.2. Effects of atmospheric winds on ice floe kinematics

While our analysis primarily focused on sea ice-ocean interactions, surface wind drag also influences ice floe motions in practical scenarios. Strong winds predominantly exert force on ice floes, potentially weakening the kinematic relationship to ocean vorticity and increasing uncertainty when inferring this information. Here, we investigate the effect of atmospheric winds on the rotational relationship between ice floes and the underlying ocean eddies by incorporating the surface wind drag term in equations (2.9) and (2.10) into our analysis.

In general, atmospheric winds have larger length scales compared to upper-ocean eddies, potentially causing ice floes to trace straight trajectories rather than curved ones (Lopez-Acosta 2021; Manucharyan *et al.* 2022a). Thus, we considered unidirectional atmospheric winds with consistent positive speeds across the entire domain in both the zonal and

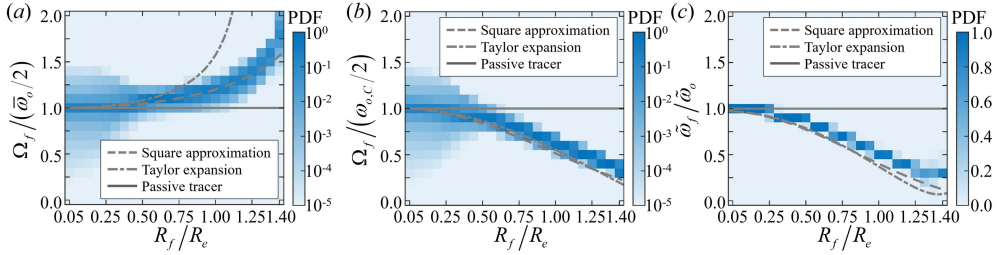


Figure 12: Motion of trapped ice floes in a TG vortex with low winds. PDF of ice floe rotation rate, Ω_f , normalized by the (a) averaged ocean vorticity over the floe area, $\bar{\omega}_o$, and the (b) ocean vorticity at the floe center of mass, $\omega_{o,C}$, and (c) of the ratio between averaged ocean vorticity estimate of the trajectory-enclosed region, $\bar{\omega}_f$, and true averaged ocean vorticity of the same region, $\bar{\omega}_o$, for different floe-eddy size ratios. The wind stress to ocean stress ratio is $\tau_a/\tau_o = 0.10$. The simulation results are compared to analytical solutions using square-shape approximation (dashed line) and Taylor series expansion (dashed-dotted line), and the passive tracer case (solid line).

meridional directions. These winds do not directly affect the rotation of ice floes under homogeneous conditions (i.e., uniform surface roughness and thickness within floes). However, unidirectional winds influence the translational motion of the ice floes, leading to increased discrepancies between their rotations and the rotations of the underlying ocean.

We investigated the motion of ice floes under weak and strong wind conditions. In low winds, ice floes tend to remain within the vortex cell. In these cases, surface wind stress to surface ocean stress ratios, $\tau_{a,ref}/\tau_{o,ref}$, range from 0 to 0.1, and wind velocities have magnitudes from 0 to 2.5 m/s. Here, the stress ratio is calculated relative to zero ice floe speed. As wind speeds increase, the influence of wind forcing on ice floe motion becomes more significant, leading to ice floes escaping the vortex cell and a notable decrease in the number of trapped ice floes, especially the large floes. In high winds, stress ratios range from 0.2 to 2.0, and wind speeds vary from 2.5 to 10.6 m/s, corresponding to observed wind speeds in the MIZ (Kozlov *et al.* 2019; Kozlov & Atadzhanova 2022).

In low wind scenarios ($\tau_{a,ref}/\tau_{o,ref} = 0.1$), the PDFs of the normalized rotation rates and the ratios between averaged ocean vorticity estimates and true ocean vorticities exhibit similar peaks and distributions (figure 12) compared to those under zero wind conditions (figures 4 and 6). For normalized rotation rates, distributions become more dispersed for most floe-eddy size ratios, with peaks slightly shifting toward higher values due to wind forcing deforming ice floe trajectories toward cell boundaries. In addition, the analytical relations (3.4)–(3.7) and (3.17) align well with PDF peaks, demonstrating the potential applicability of these derived relations under low wind conditions.

In high winds, the effects of surface wind drag on the rotational relationship vary depending on the floe-eddy size ratios (figure 13). Note that all ice floes are considered in the analyses. For $R_f/R_e = 0.1$, the effects of wind forcing on the rotation rate normalized by the averaged ocean vorticity are negligible (figure 13a). However, wind forcing marginally decreases the peaks of the PDFs and results in slightly more dispersed distributions (figure 13b). As the floe-eddy size ratio increases, the effects of wind forcing become more pronounced, resulting in skewed distributions. For $R_f/R_e = 0.5$ and 1.0, the PDF peaks of rotation rates normalized by the averaged ocean vorticity shift toward greater values (figures 13c, e), whereas the peaks of rotation rates normalized by the center-of-mass ocean vorticity shift toward lower values (figures 13d, f). The peak values in both cases decrease, and the distributions become more dispersed as the stress ratio increases from 0.1 to 0.5. Beyond this range, the PDFs begin to

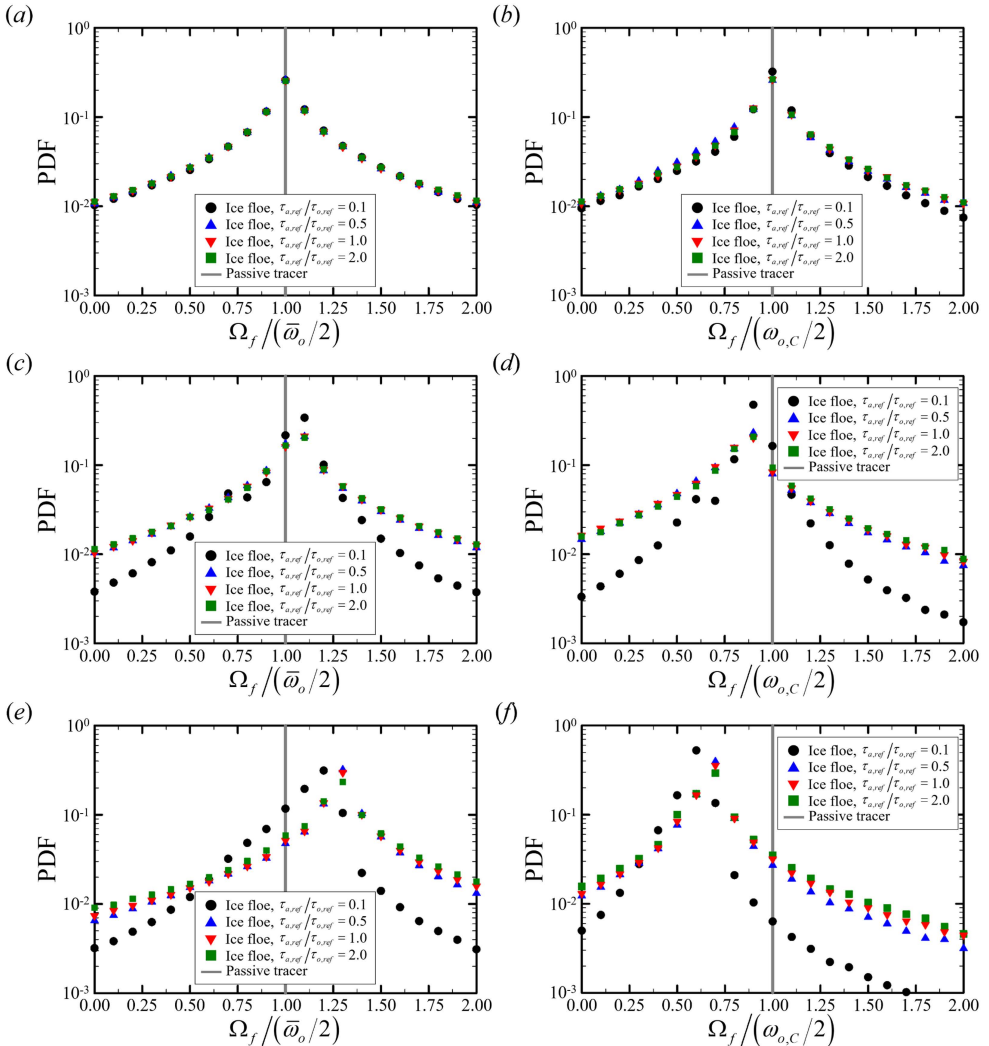


Figure 13: Motion of trapped ice floes in a TG vortex with high winds. PDF of ice floe rotation rate, Ω_f , normalized by the (a, c, e) averaged ocean vorticity over the floe area, $\bar{\omega}_o$, and the (b, d, f) ocean vorticity at the floe center of mass, $\omega_{o,C}$, for different wind stress to ocean stress ratios, $\tau_{a,ref}/\tau_{o,ref} = 0.1$ (black circle), 0.5 (blue up-pointing triangle), 1.0 (red down-pointing triangle), 2.0 (green square). The floe-eddy size ratios are $R_f/R_e = (a, b) 0.1$, (c, d) 0.5, (e, f) 1.0. The simulation results are compared to the passive tracer case (solid line).

converge, showing minor differences in the distribution. The peaks slightly decrease, and the distributions become more dispersed at larger stress ratios.

Overall, the wind breaks off the influence of ocean eddies on ice floe rotation, with the effect being most pronounced under strong wind conditions. In such cases, ice floes tend to move around and along the boundaries of the vortex cell, where ocean and wind stresses are comparable, resulting in skewed distributions of normalized rotation rates. At the same stress ratios, larger floes show significant changes in the peaks and distributions of their rotation rates due to their greater coverage of the flow field.

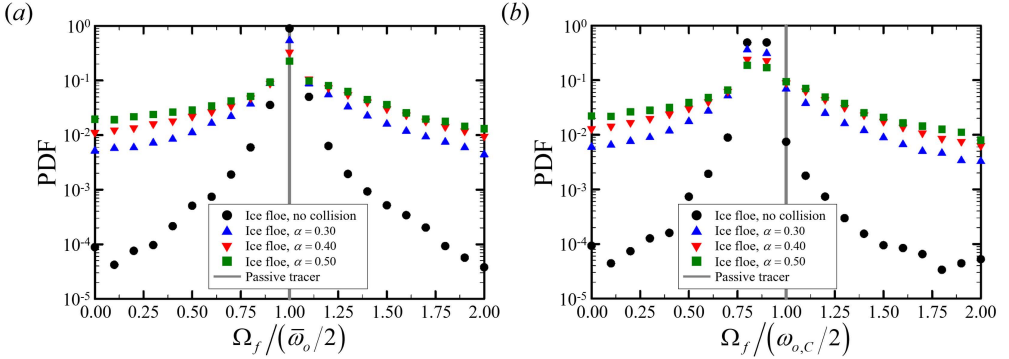


Figure 14: Motion of ice floes with collisions in a TG vortex. PDF of ice floe rotation rate, Ω_f , normalized by the (a) averaged ocean vorticity over the floe area, $\bar{\omega}_o$, and the (b) ocean vorticity at the floe center of mass, $\omega_{o,C}$, for different sea ice concentrations, $\alpha = 0.30$ (blue up-pointing triangle), 0.40 (red down-pointing triangle), and 0.50 (green square). The floe-eddy size ratio is $R_f/R_e = 0.5$. The results are compared to the freely drifting floes (black circles) and the passive tracer case (solid lines).

4.3. Effects of floe-floe collisions on ice floe kinematics

Ice floes with no collisions are typically found in regions with low sea ice concentrations. In contrast, in areas of higher sea ice concentrations, floe-floe collisions become more common due to the densely packed distribution of ice floes (Leppäranta 2011; Brunette *et al.* 2022) affecting floe rotations (Brenner *et al.* 2023). These collisions exert contact forces that weaken the connection between ice floes and the underlying ocean, introducing noise into the estimation of ocean information through ice floe motions. In this section, we explored the effects of floe-floe collisions on the rotational relationship between ice floes and the underlying ocean to assess the feasibility of using ice floes with collisions for inferring ocean kinematics.

Simulations were conducted with 2,000 randomly released ice floes, and rotation rate measurements began once the overlapping areas between ice floes were reduced to less than 10% of their total area. Sea ice concentration was calculated as the total ice floe area divided by the size of the smallest rectangular domain confining all ice floes over the simulation time. Since the domain size is determined by the instantaneous positions of the ice floes, sea ice concentration can vary slightly over time. Thus, the time-averaged sea ice concentration was used to represent each simulation. In equations (2.7) and (2.8), the contact forces, $\mathbf{F}_{j,k}$, and the corresponding torques, $\mathbf{r}'_{j,k} \times \mathbf{F}_{j,k}$, were incorporated into the simulations. The simulation parameters are consistent with those described for ice floes in the BG MIZ, as detailed in Manucharyan & Montemuro (2022b) and summarized in table 1. For the ice floe setup, the total of 2,000 ice floes was divided into smaller subsets to ensure that the number of collisions remained within specified ranges of interest while maintaining the desired sea ice concentration. Similar to the strong wind cases (§4.2), the simulated ice floes exhibited significant deviations from the closed-loop patterns observed in the idealized cases due to collisions and thus all results were indiscriminately considered.

We examined the PDFs of normalized ice floe rotation rates for different sea ice concentrations, α , and compared them to floes with no collisions (figure 14). As a representative case, we selected floes with $R_f/R_e = 0.5$, showing a clear peak in the PDFs. Sea ice concentrations ranging from $\alpha = 0.3$ to 0.5 were considered, reflecting typical moderate values in the MIZ, where concentrations range from $\alpha = 0.15$ to 0.80 . Overall, the PDF peaks occur at the same rotation rates for different concentrations, but higher concentrations

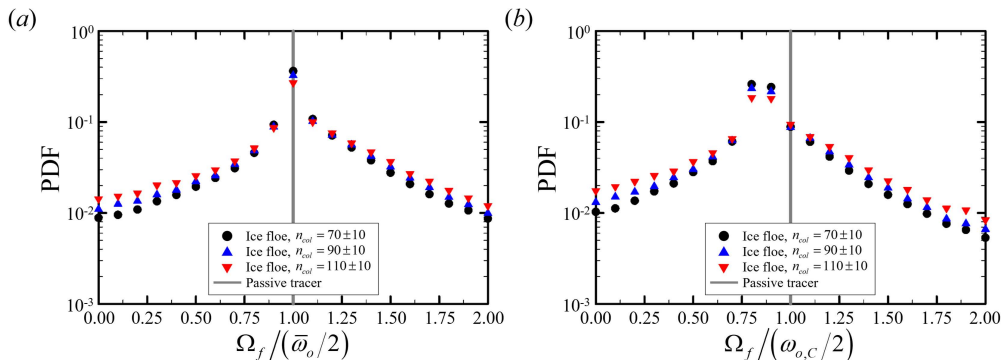


Figure 15: Motion of ice floes with collisions in a TG vortex. PDF of ice floe rotation rate, Ω_f , normalized by the (a) averaged ocean vorticity over the floe area, $\bar{\omega}_o$, and the (b) ocean vorticity at the floe center of mass, $\omega_{o,C}$ for different collision count ranges, $n_{col} = 70 \pm 10$ (black circle), 90 ± 10 (blue up-pointing triangle), and 110 ± 10 (red down-pointing triangle). The floe-eddy size ratio is $R_f/R_e = 0.5$. The results are compared to the passive tracer case (solid lines).

lead to more dispersed distributions. For rotation rates normalized by the averaged ocean vorticity, the PDF peak decreases from 0.89 (no collision case) to 0.22 ($\alpha = 0.5$) (figure 14a). Similarly, for rotation rates normalized by the center-of-mass vorticity, the PDF peak decreases from 0.49 (no collision case) to 0.19 ($\alpha = 0.5$) (figure 14b). These changes are caused by increasing collision counts at higher concentrations, which reduce the influence of ocean vorticity on ice floe rotation. The average collision count increases from zero (no-collision case) to 160 ($\alpha = 0.5$). Despite these changes, the distributions retain their shapes across different concentrations, as collisions show no directional bias in altering floe rotation.

While sea ice concentration represents the overall fraction of ice floes in the domain, collision count reflects the extent of contact forces and corresponding torques affecting ice floe motions. We compared the PDFs of normalized rotation rates for cases with different collision counts, $n_{col} = 70 \pm 10, 90 \pm 10, 110 \pm 10$, at $R_f/R_e = 0.5$ to assess the influence of floe-floe collisions (figure 15). Within each simulation run, the collision counts vary over time and only the time ranges corresponding to the selected collision counts were considered for the analysis. The PDFs consistently peak at the same rotation rates for different collision counts but become increasingly dispersed as collision counts rise. This behavior aligns with the trends observed for different sea ice concentrations, where higher concentrations generally coincide with more frequent collisions, assuming constant floe sizes.

Lastly, we explored the impacts of floe-eddy size ratios for the same collision count ranges. While sea ice concentration can be maintained through various combinations of floe sizes and the number of floes, it represents only the combined effects of these factors and is insufficient as a standalone control parameter. Instead, we used collision count as a control parameter to assess the influence of floe-eddy size ratios on ice floe rotation rates. The PDFs of normalized rotation rates for different floe-eddy size ratios were compared in the collision count range $n_{col} = 70 \pm 10$ (figure 16). Overall, the distributions exhibit qualitatively similar trends to the free-drifting cases (figure 4). The PDFs of floe rotation rates normalized by the averaged ocean vorticity exhibit distinct peak values and distributions for different floe-eddy size ratios (figure 16a). At $R_f/R_e = 0.1$, the PDF peaks at unity but has a more dispersed distribution compared to $R_f/R_e = 0.5$, where the PDF also peaks at unity. As R_f/R_e increases to 1.0, the PDF peak shifts to 1.1. The PDFs of floe rotation rates normalized by the center-of-mass

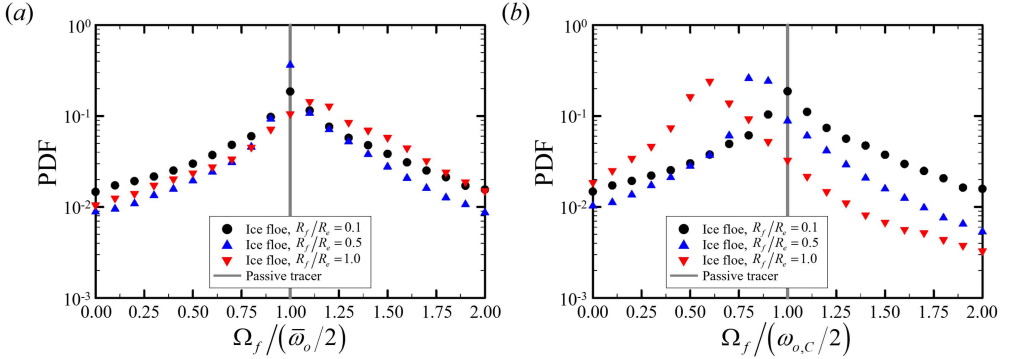


Figure 16: Motion of ice floes with collisions in a TG vortex. PDF of ice floe rotation rate, Ω_f , normalized by the (a) averaged ocean vorticity over the floe area, $\bar{\omega}_o$, and the (b) ocean vorticity at the floe center-of-mass, $\omega_{o,C}$ for different floe-eddy size ratios, $R_f/R_e = 0.1$ (black circle), 0.5 (blue up-pointing triangle), and (red down-pointing triangle) 1.0 . The collision count range is $n_{col} = 70 \pm 10$. The results are compared to the passive tracer case (solid lines).

ocean vorticity peak at lower rotation rates and show greater skewness for larger R_f/R_e (figure 16b).

5. Conclusion

We quantified the kinematic relationship between ocean eddies with surface expression and floes trapped within their cores and derived analytical relations linking their rotations and velocities, with floe-eddy size ratios as a key parameter in the analysis. Our results show that ice floes can act as vorticity meters of the ocean even though the combined effects of floe inertia and the filtering effect of ocean information over the floe area produce differences between direct measurements of ocean velocities and rotations and estimates derived from ice floe observations. These findings and the derived analytical relations demonstrate the potential applicability of our methodology for inferring ocean eddy characteristics from ice floe remote sensing measurements.

We began our analysis with a TG vortex, employing two distinct vorticity metrics: averaged ocean vorticity over the floe area and ocean vorticity at the floe center of mass. Our analysis revealed that individual ice floes typically follow closed-loop trajectories, driven by the interplay of sea ice-ocean drag and a resultant force comprising the pressure gradient force due to sea surface tilt and the Coriolis force. Along these trajectories, the rotation rates and velocities of ice floes show oscillatory behavior, undergoing alternating periods of acceleration and deceleration relative to the equilibrium values of force and torque. The rotation rate normalized by the averaged ocean vorticity increases with increasing floe-eddy size ratio for both centered and off-centered ice floes. This trend arises from the gradual decrease in local ocean vorticity from the center of the TG vortex toward its boundaries. Ice floes behave as passive tracers when $R_f/R_e \leq 0.7$; however, as the floe-eddy size ratio increases to 1.4 , the PDF peaks of rotation rates normalized by the averaged ocean vorticity shift toward higher values, reaching approximately 1.8 . Around $R_f/R_e \approx 0.5$, the distribution narrows and exhibits higher peaks, indicating that a solid body rotation approximation effectively describes ice floe motion within this range. Conversely, the rotation rate normalized by the center-of-mass ocean vorticity decreases for large floe-eddy size ratios. The velocities of ice floes were also used to estimate the averaged ocean vorticity within

regions enclosed by their trajectories. These estimates were smaller than the true ocean vorticity of the same region; their ratios can be described by the relationship between ice floe and ocean velocities.

To further understand these dynamics, we derived analytical relations for ice floe rotation rates and velocities using the Taylor series expansion and the square-shape approximation. While the Taylor series expansion agrees well with the PDF peaks for small floe-eddy size ratios ($R_f/R_e \leq 0.5$), the square-shape approximation aligns closely with the PDF peaks across a broader range of size ratios. Analytical relations for the ratio between the averaged ocean vorticity estimate and true ocean vorticity also show good agreement with the PDF peaks. These relations were applied to a more realistic ocean eddy field obtained from a two-layer QG model. The trends observed in the TG vortex are also evident in the QG flow field when floe size is normalized by the trajectory-derived length scale. As the normalized floe size increases, the rotation rates normalized by the averaged ocean vorticity increase, while those normalized by the center-of-mass ocean vorticity decrease. The derived relations closely match the PDF peaks for normalized rotation rates, demonstrating their potential applicability in inferring ocean kinematics through ice floe motions.

We closed our study by exploring other factors influencing the rotational relationship between ice floes and the underlying ocean, such as ice floe thickness, atmospheric winds, and floe-floe collisions. For ice floe thicknesses ranging from 0.1 to 1 m, we found that thicker floes exhibit reduced PDF peaks and more dispersed distributions due to increased floe inertia. Interestingly, the impact of varying floe thickness lessens with increasing floe-eddy size ratios and becomes negligible at $R_f/R_e = 0.5$. We also examined atmospheric wind forcing under low and high wind conditions. Under low wind conditions, wind-sea ice stresses have a minor effect on the normalized rotation rates, causing their PDF peaks to shift slightly to higher values. In high wind conditions, the PDFs of normalized rotation rates are skewed as stress ratios increase. The PDFs converge under larger stress ratios for increasing floe-eddy size ratios ($R_f/R_e = 0.1$ to 1.0). Finally, we investigated the impact of floe-floe collisions, which weaken the rotational link between ice floes and the underlying ocean. For $R_f/R_e = 0.5$, higher sea ice concentrations and larger collision counts lead to reduced PDF peaks and more dispersed distributions. When considering a fixed collision count ($n_{col} = 70 \pm 10$), the PDFs for different floe-eddy size ratios exhibit trends consistent with those observed in free-drifting cases.

Our findings and analytical relations provide a new framework for estimating local ocean vorticity with associated uncertainties. By incorporating Lagrangian observations of ice floe trajectories, rotation rates, velocities, and shapes, the analytical relations can provide locally averaged ocean vorticities and velocities. Furthermore, PDFs of ice floe rotation rates enable the assessment of uncertainties in estimated ocean information. While the derived relations effectively describe the ice floe-ocean relationship, practical applications require further consideration of factors such as strong ocean currents, varying eddy and ice floe shapes, and eddy evolution, which must be fully captured in our idealized setup. Uncertainties due to ice floe thickness, atmospheric winds, and floe-floe collisions also require further study. Nonetheless this study lays a foundation for a robust framework to characterize eddies from satellite remote sensing observations of sea ice, which can easily be extended beyond the Beaufort Gyre to include MIZ eddies in the Arctic and Antarctic Oceans.

Funding. M.K. and M.M.W were supported by the Office of Naval Research (ONR) Arctic Program (N00014-20-1-2753, N00014-22-1-2741, and N00014-22-1-2722), the ONR Young Investigator Program (N00014-24-1-2283), and the National Aeronautics and Space Administration Science of Terra, Aqua, and Suomi-NPP Program (80NSSC22K0620). M.K., M.M.W, and G.E.M were also supported by the ONR Multidisciplinary University Research Initiatives Program (N00014-23-1-2014).

Declaration of interests. The authors report no conflict of interest.

Author ORCIDs. M. Kim, <https://orcid.org/0000-0002-8613-0206>; G.E. Manucharyan, <https://orcid.org/0000-0001-7959-2675>; M.M. Wilhelmus, <https://orcid.org/0000-0002-3980-2620>.

Appendix A. Identification of ice floes trapped by an ocean eddy

We leverage ice floe trajectories resembling closed loops to identify floes trapped in an eddy core, in agreement with conventional eddy detection algorithms (Chelton *et al.* 2011; Mason *et al.* 2014). Several physical criteria were established for selecting closed-loop trajectories based on previous work using processed satellite remote sensing observations via the Ice Floe Tracker algorithm (Lopez-Acosta *et al.* 2019; Lopez-Acosta 2021). First, the curvatures of all daily segments along the trajectory must be of the same sign, indicating that an ice floe has been rotating clockwise or counterclockwise. Then, considering a nominal eddy size of 20 km, trajectory curvatures are evaluated as they should surpass a predefined threshold typically set at $0.05 \text{ [km}^{-1}\text{]}$. A third condition is set by the ratio of the arc length along the trajectory to the distance between the initial and final points. This value must exceed a specific threshold, typically set at 3, based on the geometry of a half-closed circular loop. Finally, only trajectories with lifetimes greater than four simulation days are considered to ensure adequate data points. Only trajectories meeting all four criteria are classified as closed-loop trajectories.

Appendix B. Effects of ice-ocean stress parametrization on the relationship between ocean vorticity and the rotation rate of ice floes

The idealized Rankin (RK) vortex was used to examine the effect of ice-ocean stress on the rotational relationship between ice floes and the underlying ocean. In the RK vortex, vorticity remains constant within the core region ($r \leq R_e$) and is zero in the outer region. The velocity field is defined as $u_\theta = \Omega_f r$ for $r \leq R_e$ and $u_\theta = \Omega_f (R_e^2/r)$ for $r > R_e$, where u_θ is the azimuthal velocity. By representing the sea ice-ocean drag term using a linear drag law in equations (2.8) and (2.10), we can derive the relation for ice floe rotation as follows:

$$\Omega_f = \frac{\bar{\omega}_o}{2} \quad \text{for } R_f \leq R_e, \quad \Omega_f = \frac{\bar{\omega}_o}{2} \left[2 - \left(\frac{R_e}{R_f} \right)^2 \right] \quad \text{for } R_f > R_e, \quad (\text{B } 1)$$

where $\bar{\omega}_o$ is the spatially averaged ocean vorticity over the floe area. For $R_f \leq R_e$, $\bar{\omega}_o = 2\Omega_f$, whereas for $R_f > R_e$, $\bar{\omega}_o = 2\Omega_f (R_e/R_f)^2$. These relations suggest that when $R_f \leq R_e$, the rotation of the ice floe mirrors the average rotation of the underlying eddies, akin to the passive tracer case. However, when $R_f > R_e$, the rotation rate increases and tends to converge toward twice the averaged ocean rotation as R_f approaches infinity. With the quadratic drag law (equation 2.6), the rotation rate of ice floes remains unchanged compared to the linear parameterization, provided that $R_f \leq R_e$. For $R_f > R_e$, the rotation rate of ice floes can be determined by solving the following algebraic equation:

$$\Omega_f^{5/2} - \Omega_f^{3/2} \left(\frac{\bar{\omega}_o}{2} \right) \left[\frac{10}{3} + \frac{4}{3} \left(\frac{R_e}{R_f} \right)^3 \right] + \Omega_f^{1/2} \left(\frac{\bar{\omega}_o}{2} \right)^2 \left[4 \left(\frac{R_e}{R_f} \right) + 5 \right] - \frac{16}{3} \left(\frac{\bar{\omega}_o}{2} \right)^{5/2} = 0, \quad (\text{B } 2)$$

where $\Omega_f = \bar{\omega}_o/2$ for $R_f = R_e$. The quadratic drag parameterization exhibits a closer fit to the simulation results compared to a linear drag (figure 17). However, the analytical relations demonstrate minimal dependence on drag parameterizations, as evidenced by the marginal error in the linear drag case.

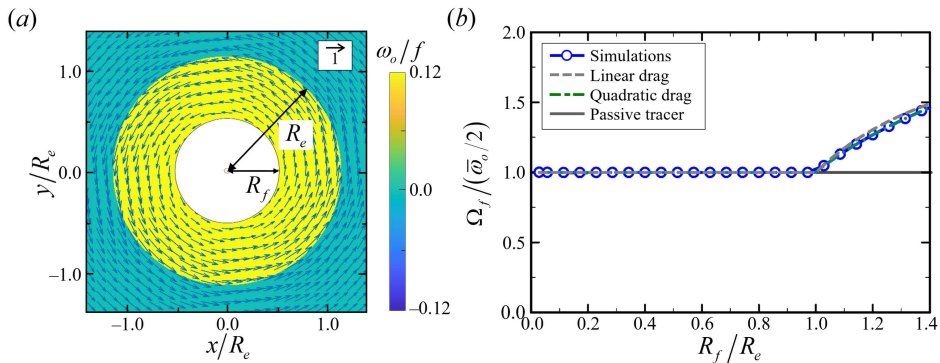


Figure 17: Motions of ice floes in a Rankine vortex field. (a) An ice floe (white circle) positioned at the center of the vortex core (yellow region), with a floe-eddy size ratio of $R_f/R_e = 0.5$. The colors and arrows in the figure correspond to the magnitude of the vorticity normalized by the Coriolis parameter and the magnitude and direction of the velocity at a given location, respectively. (b) Rotation rates of the ice floe normalized by the averaged ocean vorticity over the floe area for different floe-eddy size ratios. The simulation results are compared with the analytical relations derived using the linear (dashed line) and quadratic (dashed-dotted line) drag laws, as well as with the passive tracer case (solid line).

REFERENCES

- ABERNATHEY, R. & HALLER, G. 2018 Transport by lagrangian vortices in the eastern pacific. *J. Phys. Oceanogr.* **48** (3), 667–685.
- ADRIAN, R.J. & WESTERWEEEL, J. 2011 *Particle image velocimetry*. Cambridge University Press.
- AKSAMIT, N.O., ENCINAS-BARTOS, A.P., HALLER, G. & RIVAL, D.E. 2024 Relative fluid stretching and rotation for sparse trajectory observations. *J. Fluid Mech.* **996**, A40.
- ALLENDE, S. & BEC, J. 2023 Velocity and acceleration statistics of heavy spheroidal particles in turbulence. *J. Fluid Mech.* **967**, R4.
- VON APPEN, W.-J., BAUMANN, T.M., JANOUT, M., KOLDUNOV, N., LENN, Y.-D., PICKART, R.S., SCOTT, R.B. & WANG, Q. 2022 Eddies and the distribution of eddy kinetic energy in the arctic ocean. *Oceanogr.* **35** (3/4), 42–51.
- ARBIC, B.K., SCOTT, R.B., FLIERL, G.R., MORTEN, A.J., RICHMAN, J.G. & SHRIVER, J.F. 2012 Nonlinear cascades of surface oceanic geostrophic kinetic energy in the frequency domain. *J. Phys. Oceanogr.* **42** (9), 1577–1600.
- ARMITAGE, T.W.K., MANUCHARYAN, G.E., PETTY, A.A., KWOK, R. & THOMPSON, A.F. 2020 Enhanced eddy activity in the beaufort gyre in response to sea ice loss. *Nat. Commun.* **11** (1), 761.
- BOFFETTA, G. & ECKE, R.E. 2012 Two-dimensional turbulence. *Annu. Rev. Fluid Mech.* **44** (1), 427–451.
- BORDOLOI, A.D. & VARIANO, E. 2017 Rotational kinematics of large cylindrical particles in turbulence. *J. Fluid Mech.* **815**, 199–222.
- BRANDT, L. & COLETTI, F. 2022 Particle-laden turbulence: progress and perspectives. *Annu. Rev. Fluid Mech.* **54** (1), 159–189.
- BRENNER, S., HORVAT, C., HALL, P., LO PICCOLO, A., FOX-KEMPER, B., LABBÉ, S. & DANSEREAU, V. 2023 Scale-dependent air-sea exchange in the polar oceans: Floe-floe and floe-flow coupling in the generation of ice-ocean boundary layer turbulence. *Geophys. Res. Lett.* **50** (23), e2023GL105703.
- BRENNER, S., RAINVILLE, L., THOMSON, J., COLE, S. & LEE, C. 2021 Comparing observations and parameterizations of ice-ocean drag through an annual cycle across the beaufort sea. *J. Geophys. Res. Oceans* **126** (4), e2020JC016977.
- BRUNETTE, C., TREMBLAY, L.B. & NEWTON, R. 2022 A new state-dependent parameterization for the free drift of sea ice. *The Cryosphere* **16** (2), 533–557.
- CAFLISCH, R.E. 1998 Monte carlo and quasi-monte carlo methods. *Acta Numer.* **7**, 1–49.
- CALLIES, J., FERRARI, R., KLYMAK, J.M. & GULA, J. 2015 Seasonality in submesoscale turbulence. *Nat. Commun.* **6** (1), 6862.

- CASSIANIDES, A., LIQUE, C. & KOROSOV, A. 2021 Ocean eddy signature on sar-derived sea ice drift and vorticity. *Geophys. Res. Lett.* **48** (6), e2020GL092066.
- CHELTON, D.B., SCHLAX, M.G. & SAMELSON, R.M. 2011 Global observations of nonlinear mesoscale eddies. *Prog. Oceanogr.* **91** (2), 167–216.
- COLE, S. T., TIMMERMANS, M.-L., TOOLE, J. M., KRISHFIELD, R. A. & THWAITES, F. T. 2014 Ekman veering, internal waves, and turbulence observed under arctic sea ice. *J. Phys. Oceanogr.* **44** (5), 1306–1328.
- COMISO, J.C. 2012 Large decadal decline of the arctic multiyear ice cover. *J. Clim.* **25** (4), 1176–1193.
- COVINGTON, J., CHEN, N. & WILHELMUS, M.M. 2022 Bridging gaps in the climate observation network: A physics-based nonlinear dynamical interpolation of lagrangian ice floe measurements via data-driven stochastic models. *J. Adv. Model. Earth Syst.* **14** (9), e2022MS003218.
- DAUXOIS, T., PEACOCK, T., BAUER, P., CAULFIELD, C.P., CENEDESE, C., GORLÉ, C., HALLER, G., IVEY, G.N., LINDEN, P.F., MEIBURG, E., PINARDI, N., VRIEND, N.M. & WOODS, A.W. 2021 Confronting grand challenges in environmental fluid mechanics. *Phys. Rev. Fluids* **6** (2), 020501.
- DENG, R., WANG, C.-H. & SMITH, K.A. 2006 Bubble behavior in a taylor vortex. *Phys. Rev. E* **73** (3), 036306.
- DIBARBOURE, G., ANADON, C., BRIOL, F., CADIER, E., CHEVRIER, R., DELEPOULLE, A., FAUGÈRE, Y., LALOUE, A., MORROW, R., PICOT, N., PRANDI, P., PUJOL, M.-I., RAYNAL, M., TREBOUTTE, A. & UBELMANN, C. 2024 Blending 2d topography images from swot into the altimeter constellation with the level-3 multi-mission duacs system. *EGUsphere[preprint]* **2024**, 1–64.
- DONG, C., LIU, Y., LUMPKIN, R., LANKHORST, M., CHEN, D., MCWILLIAMS, J. C. & GUAN, Y. 2011 A scheme to identify loops from trajectories of oceanic surface drifters: An application in the kuroshio extension region. *J. Atmos. Ocean. Technol.* **28** (9), 1167–1176.
- FERRARI, R. & WUNSCH, C. 2009 Ocean circulation kinetic energy: Reservoirs, sources, and sinks. *Annu. Rev. Fluid Mech.* **41** (1), 253–282.
- GUPTA, M., GÜRCAN, E. & THOMPSON, A.F. 2024 Eddy-induced dispersion of sea ice floes at the marginal ice zone. *Geophys. Res. Lett.* **51** (2), e2023GL105656.
- GUPTA, M. & THOMPSON, A.F. 2022 Regimes of sea-ice floe melt: Ice-ocean coupling at the submesoscales. *J. Geophys. Res. Oceans* **127** (9), e2022JC018894.
- HAAS, C. & DRUCKENMILLER, M. 2009 Ice thickness and roughness measurements. In *Field techniques for sea ice research* (ed. H. Eicken & M. Salganek), chap. 3.2, pp. 49–116. Fairbanks: University of Alaska Press.
- HALLER, GEORGE 2005 An objective definition of a vortex. *J. Fluid Mech.* **525**, 1–26.
- HALLER, G., HADJIGHASEM, A., FARAZMAND, M. & HUHN, F. 2016 Defining coherent vortices objectively from the vorticity. *J. Fluid Mech.* **795**, 136–173.
- HARMS, T.D., BRUNTON, S.L. & MCKEON, B.J. 2023 Lagrangian gradient regression for the detection of coherent structures from sparse trajectory data. *arXiv preprint arXiv:2310.10994*.
- HOWELL, S.E.L., BABB, D.G., LANDY, J.C., MOORE, G.W.K., MONTPETIT, B. & BRADY, M. 2023 A comparison of arctic ocean sea ice export between nares strait and the canadian arctic archipelago. *J. Geophys. Res. Oceans* p. e2023JC019687.
- HUNKINS, K.L. 1974 Subsurface eddies in the arctic ocean. In *Deep-Sea Research*, , vol. 21, pp. 1017–1033. Elsevier.
- ISERN-FONTANET, J., FONT, J., GARCÍA-LADONA, E., EMELIANOV, M., MILLOT, C. & TAUPIER-LETAGE, I. 2004 Spatial structure of anticyclonic eddies in the algerian basin (mediterranean sea) analyzed using the okubo–weiss parameter. *Deep-Sea Res. II: Top. Stud. Oceanogr.* **51** (25–26), 3009–3028.
- JAYARAM, R., JIE, Y., ZHAO, L. & ANDERSSON, H.I. 2020 Clustering of inertial spheres in evolving taylor–green vortex flow. *Phys. Fluids* **32** (4).
- JOHANNESSEN, J.A., JOHANNESSEN, O.M., SVENDSEN, E., SHUCHMAN, R., MANLEY, T., CAMPBELL, W.J., JOSBERGER, E.G., SANDVEN, S., GASCARD, J.C., OLAUSSEN, T., DAVIDSON, K. & VAN LEER, J. 1987 Mesoscale eddies in the fram strait marginal ice zone during the 1983 and 1984 marginal ice zone experiments. *J. Geophys. Res. Oceans* **92** (C7), 6754–6772.
- KLEIN, P., LAPEYRE, G., SEGELMAN, L., QIU, B., FU, L.-L., TORRES, H., SU, Z., MENEMENLIS, D. & LE GENTIL, S. 2019 Ocean-scale interactions from space. *Earth Planet. Sci.* **6** (5), 795–817.
- KOZLOV, I.E., ARTAMONOVA, A.V., MANUCHARYAN, G.E. & KUBRYAKOV, A.A. 2019 Eddies in the western arctic ocean from spaceborne sar observations over open ocean and marginal ice zones. *J. Geophys. Res. Oceans* **124** (9), 6601–6616.
- KOZLOV, I.E. & ATADZHANOVA, O.A. 2022 Eddies in the marginal ice zone of fram strait and svalbard from spaceborne sar observations in winter. *Remote Sens.* **14** (1), 134.
- KOZLOV, I.E., PLOTNIKOV, E.V. & MANUCHARYAN, G.E. 2020 Brief communication: Mesoscale and

- submesoscale dynamics in the marginal ice zone from sequential synthetic aperture radar observations. *The Cryosphere* **14** (9), 2941–2947.
- KRISHFIELD, R. A., PROSHUTINSKY, A., TATEYAMA, K., WILLIAMS, W. J., CARMACK, E. C., McLAUGHLIN, F. A. & TIMMERMANS, M. L. 2014 Deterioration of perennial sea ice in the beaufort gyre from 2003 to 2012 and its impact on the oceanic freshwater cycle. *J. Geophys. Res. Oceans* **119** (2), 1271–1305.
- KUBRYAKOV, A.A., KOZLOV, I.E. & MANUCHARYAN, G.E. 2021 Large mesoscale eddies in the western arctic ocean from satellite altimetry measurements. *J. Geophys. Res. Oceans* **126** (5), e2020JC016670.
- KWOK, R. & ROTHROCK, D.A. 2009 Decline in arctic sea ice thickness from submarine and icesat records: 1958–2008. *Geophys. Res. Lett.* **36** (15).
- LEPPÄRANTA, MATTI 2011 *The drift of sea ice*. Springer Science & Business Media.
- LIU, C., WANG, Q., DANILOV, S., KOLDUNOV, N., MÜLLER, V., LI, X., SIDORENKO, D. & ZHANG, S. 2024 Spatial scales of kinetic energy in the arctic ocean. *J. Geophys. Res. Oceans* **129** (3), e2023JC020013.
- LIU, T. & ABERNATHEY, R. 2023 A global lagrangian eddy dataset based on satellite altimetry. *Earth Syst. Sci. Data Discuss.* **2022**, 1–20.
- LOPEZ-ACOSTA, R. 2021 Sea ice drift in arctic marginal ice zones derived from optical satellite imagery. PhD thesis, University of California, Riverside.
- LOPEZ-ACOSTA, R., SCHODLOK, M.P. & WILHELMUS, M.M. 2019 Ice floe tracker: An algorithm to automatically retrieve lagrangian trajectories via feature matching from moderate-resolution visual imagery. *Remote Sens. Environ.* **234**, 111406.
- MA, B., STEELE, M. & LEE, C. M. 2017 Ekman circulation in the arctic ocean: Beyond the beaufort gyre. *J. Geophys. Res. Oceans* **122** (4), 3358–3374.
- MANUCHARYAN, G.E., LOPEZ-ACOSTA, R. & WILHELMUS, M.M. 2022a Spinning ice floes reveal intensification of mesoscale eddies in the western arctic ocean. *Sci. Rep.* **12** (1), 7070.
- MANUCHARYAN, G.E. & MONTEMURO, B.P. 2022b Subzero: A sea ice model with an explicit representation of the floe life cycle. *J. Adv. Model. Earth Syst.* **14** (12), e2022MS003247.
- MANUCHARYAN, G.E. & STEWART, A.L. 2022 Stirring of interior potential vorticity gradients as a formation mechanism for large subsurface-intensified eddies in the beaufort gyre. *J. Phys. Oceanogr.* **52** (12), 3349–3370.
- MANUCHARYAN, G.E. & THOMPSON, A.F. 2022c Heavy footprints of upper-ocean eddies on weakened arctic sea ice in marginal ice zones. *Nat. Commun.* **13** (1), 2147.
- MASON, E., PASCUAL, A. & McWILLIAMS, J.C. 2014 A new sea surface height-based code for oceanic mesoscale eddy tracking. *J. Atmos. Ocean. Technol.* **31** (5), 1181–1188.
- MCPHEE, M. G. 2012 Advances in understanding ice–ocean stress during and since aidjex. *Cold Reg. Sci. Technol.* **76**, 24–36.
- MONTEMURO, B.P. & MANUCHARYAN, G.E. 2023 Subzero: a discrete element sea ice model that simulates floes as evolving concave polygons. *J. Open Source Softw.* **8** (88), 5039.
- MORROW, R. & LE TRAON, P.-Y. 2012 Recent advances in observing mesoscale ocean dynamics with satellite altimetry. *Adv. Space Res.* **50** (8), 1062–1076.
- MORTENSEN, P.H., ANDERSSON, H.I., GILLISSEN, J.J.J. & BOERSMA, B.J. 2007 Particle spin in a turbulent shear flow. *Phys. Fluids* **19** (7), 078109.
- MOWLAVI, S., SERRA, M., MAIORINO, E. & MAHADEVAN, L. 2022 Detecting lagrangian coherent structures from sparse and noisy trajectory data. *J. Fluid Mech.* **948**, A4.
- MÜLLER, V., WANG, Q., KOLDUNOV, N., DANILOV, S., SIDORENKO, D. & JUNG, T. 2024 Variability of eddy kinetic energy in the eurasian basin of the arctic ocean inferred from a model simulation at 1-km resolution. *J. Geophys. Res. Oceans* **129** (3), e2023JC020139.
- OKUBO, A. 1970 Horizontal dispersion of floatable particles in the vicinity of velocity singularities such as convergences. In *Deep-Sea Res.*, , vol. 17, pp. 445–454. Elsevier.
- OUELLETTE, N.T., O'MALLEY, P.J.J. & GOLLUB, J.P. 2008 Transport of finite-sized particles in chaotic flow. *Phys. Rev. Lett.* **101** (17), 174504.
- OUTRATA, O., PAVELKA, M., HRON, J., LA MANTIA, M., POLANCO, J.I. & KRSTULOVIC, G. 2021 On the determination of vortex ring vorticity using lagrangian particles. *J. Fluid Mech.* **924**, A44.
- PÉREZ-MUÑUZURI, V. & HUHN, F. 2013 Path-integrated lagrangian measures from the velocity gradient tensor. *Nonlinear Process. Geophys.* **20** (6), 987–991.
- PNYUSHKOV, A., POLYAKOV, I.V., PADMAN, L. & NGUYEN, A.T. 2018 Structure and dynamics of mesoscale eddies over the laptev sea continental slope in the arctic ocean. *Ocean Sci.* **14** (5), 1329–1347.
- QIAO, J., DENG, R. & WANG, C.-H. 2014 Droplet behavior in a taylor vortex. *Int. J. Multiph. Flow* **67**, 132–139.

- QIAO, J., DENG, R. & WANG, C.-H. 2015 Particle motion in a Taylor vortex. *Int. J. Multiph. Flow* **77**, 120–130.
- RAMPAL, P., WEISS, J. & MARSAN, D. 2009 Positive trend in the mean speed and deformation rate of arctic sea ice, 1979–2007. *J. Geophys. Res. Oceans* **114** (C5).
- ROLPH, R.J., FELTHAM, D.L. & SCHRÖDER, D. 2020 Changes of the arctic marginal ice zone during the satellite era. *The Cryosphere* **14** (6), 1971–1984.
- STRONG, C. & RIGOR, I.G. 2013 Arctic marginal ice zone trending wider in summer and narrower in winter. *Geophys. Res. Lett.* **40** (18), 4864–4868.
- ŠVANČARA, P., PAVELKA, M. & LA MANTIA, M. 2020 An experimental study of turbulent vortex rings in superfluid 4He . *J. Fluid Mech.* **889**, A24.
- TEE, Y.H. & LONGMIRE, ELLEN K. 2024 Effect of fluid motions on finite spheres released in turbulent boundary layers. *Journal of Fluid Mechanics* **985**, A28.
- TIMMERMANS, M.-L. & MARSHALL, J. 2020 Understanding arctic ocean circulation: A review of ocean dynamics in a changing climate. *J. Geophys. Res. Oceans* **125** (4), e2018JC014378.
- TIMMERMANS, M.-L., TOOLE, J., PROSHUTINSKY, A., KRISHFIELD, R. & PLUEDDEMANN, A. 2008 Eddies in the Canada basin, arctic ocean, observed from ice-tethered profilers. *J. Phys. Oceanogr.* **38** (1), 133–145.
- TULLOCH, R., MARSHALL, J., HILL, C. & SMITH, K. S. 2011 Scales, growth rates, and spectral fluxes of baroclinic instability in the ocean. *J. Phys. Oceanogr.* **41** (6), 1057–1076.
- VARAKSIN, A.Y. & RYZHKOV, S.V. 2022 Vortex flows with particles and droplets (a review). *Symmetry* **14** (10), 2016.
- VOTH, G.A. & SOLDATI, A. 2017 Anisotropic particles in turbulence. *Annu. Rev. Fluid Mech.* **49** (1), 249–276.
- WERELEY, S.T. & LUEPTOW, R.M. 1999 Inertial particle motion in a Taylor-Couette rotating filter. *Phys. Fluids* **11** (2), 325–333.
- YANG, J. 2006 The seasonal variability of the arctic ocean Ekman transport and its role in the mixed layer heat and salt fluxes. *J. Clim.* **19** (20), 5366–5387.
- YANG, Y., MIN, C., LUO, H., KAUKER, F., RICKER, R. & YANG, Q. 2023 The evolution of the Fram Strait sea ice volume export decomposed by age: Estimating with parameter-optimized sea ice-ocean model outputs. *Environ. Res. Lett.* **18** (1), 014029.
- ZHAO, L., CHALLABOTLA, N.R., ANDERSSON, H.I. & VARIANO, E.A. 2015 Rotation of nonspherical particles in turbulent channel flow. *Phys. Rev. Lett.* **115** (24), 244501.
- ZHAO, M., TIMMERMANS, M.-L., COLE, S., KRISHFIELD, R. & TOOLE, J. 2016 Evolution of the eddy field in the arctic ocean's Canada basin, 2005–2015. *Geophys. Res. Lett.* **43** (15), 8106–8114.
- ZHONG, W., STEELE, M., ZHANG, J. & ZHAO, J. 2018 Greater role of geostrophic currents in Ekman dynamics in the western arctic ocean as a mechanism for Beaufort gyre stabilization. *J. Geophys. Res. Oceans* **123** (1), 149–165.